Journal of Geodesy (2026) 100:96
https://doi.org/10.1007/s00190-026-02084-3

ORIGINAL ARTICLE

An evaluation of global ionosphere maps for the ionospheric correction of C-band InSAR data

Xue Li[1] · Cunren Liang[1] · Jiafeng Li[2] · Kejie Chen[3]

Received: 4 October 2025 / Accepted: 31 May 2026
© Springer-Verlag GmbH Germany, part of Springer Nature 2026

Abstract

The ionosphere is often the most significant long-wavelength error source in Earth's surface motion measurement using Synthetic Aperture Radar (SAR) Interferometry (InSAR). The application of the range split-spectrum method to C-band InSAR is limited by low coherence and phase unwrapping errors. In this work, we comprehensively evaluate Global Ionosphere Maps (GIMs) for correcting ionospheric effects in C-band InSAR. The evaluation encompasses eight GIMs from the International GNSS Service (IGS), a new high-resolution GIM from the Jet Propulsion Laboratory (JPL), and the Extended Timing Annotation Dataset (ETAD) recently released by the European Space Agency (ESA). The performance of these GIMs is evaluated for correcting both individual interferograms and InSAR time series. The influence of the InSAR time series duration relative to the 11-year solar cycle is also analyzed. Moreover, an empirical adaptive scaling factor is introduced to account for the altitude difference between GNSS and SAR satellites. The results indicate that the high-resolution JPL GIM provides effective ionospheric correction for C-band InSAR. While the IGS GIMs and ETAD can improve most InSAR results, their effectiveness is limited by their temporal and spatial resolutions. Among the IGS GIMs, codg generally demonstrates the most stable and best overall performance. The performance also depends on the geographical region (related to IGS station density) and the temporal mismatch between the SAR acquisition time and the GIM product time. These evaluations not only serve to validate the current GIM products and provide useful feedback, but also motivate further improvement in the resolution of IGS GIMs.

Keywords GIMs · InSAR · Ionosphere · C-band

1 Introduction

Synthetic Aperture Radar (SAR) Interferometry (InSAR) is an essential geodetic technique for measuring Earth's surface motion, a key observable for understanding tectonic processes. Early studies employing InSAR were largely confined to small scales (Massonnet et al. 1993; Goldstein et al. 1993; Peltzer and Rosen 1995; Grandin et al. 2012). Recent advances in SAR hardware, processing algorithms, and computation capability have enabled InSAR to measure Earth's surface motion at large scales. However, most large-scale InSAR measurements still require constraints from external data, such as Global Navigation Satellite System (GNSS) measurements (Watson et al. 2022, 2024; Ou et al. 2022; Weiss et al. 2020; Tong et al. 2013; Xu et al. 2021), as these large-scale measurements are frequently contaminated by a variety of long-wavelength errors or signals, sometimes dubbed "ramps". Critically, the retrieval of long-wavelength yet small-magnitude deformations remains one of the most challenging problems in InSAR, as the signal of interest can be easily overwhelmed by these errors.

Long-wavelength errors or signals in InSAR can result from systematic and processing errors, atmospheric propagation effects including tropospheric delays (Zebker et al. 1997) and ionospheric advances (Gray et al. 2000), and other Earth's surface motions that are not of interest, such as plate motions, and tidal and loading effects. Tropospheric delays

✉ Cunren Liang
cunren.liang@pku.edu.cn

[1] Institute of Remote Sensing and Geographic Information System, School of Earth and Space Sciences, Peking University, Beijing 100871, China

[2] School of Geodesy and Geomatics, Wuhan University, Wuhan 430072, China

[3] Department of Earth and Space Sciences, Southern University of Science and Technology, Shenzhen 518055, China

Published online: 13 October 2026

and ionospheric advances represent the most significant long-wavelength signals and can be as large as meter-level values. Tropospheric delays can be largely removed using global atmospheric models (Jolivet et al. 2014). Plate motions can induce long-wavelength spatial gradients of millimeters per year over hundreds of kilometers in InSAR velocity fields (Stephenson et al. 2022), while tidal and loading effects can result in ground motions ranging from millimeters to decimeters. These signals can be precisely computed using respective models (Luzum and Petit 2012; Stephenson et al. 2022; Lemrabet et al. 2023). The magnitude of long-wavelength errors resulting from systematic and processing errors varies. In particular, orbit errors were long considered to be the dominant source of long-wavelength errors in the early days. However, they are currently not a concern for representative modern SAR satellites, as SAR and InSAR processing has become standardized and orbit data typically achieve centimeter-level precision.

Therefore, if we set aside errors associated with data quality and processing, such as decorrelation and phase unwrapping, the primary remaining source of long-wavelength error in large-scale InSAR measurements is the ionosphere. While the ionosphere was traditionally considered to primarily affect InSAR with L-band data, recent studies revealed that it can also degrade C-band InSAR results, with the severity depending on data acquisition time and location (Liang et al. 2019). The range split-spectrum method developed in recent years, a technique analogous to that routinely used for GNSS ionospheric correction, enables precise estimation of the ionospheric phase in InSAR (Rosen et al. 2010; Brcic et al. 2010; Gomba et al. 2016; Liang and Fielding 2017). However, it often fails, or is not able to precisely estimate the ionospheric phase when applied to C-band data due to low coherence and phase unwrapping errors (Liang et al. 2019), as shown in Fig. 1.

The ionospheric phase advance results from the refraction of microwaves in the ionosphere, and its magnitude is proportional to the Total Electron Content (TEC) along the signal path. TEC is primarily modulated by solar activity, which impacts many human activities, particularly those relying on electromagnetic waves. The International GNSS Service (IGS) has been routinely measuring global Vertical TEC (VTEC) using the Global GPS Network (GGN) with more than 500 dual-frequency geodetic quality receivers, and the resulting products are provided as the Global Ionosphere Maps (GIMs) (Mannucci et al. 1998). Although the spatial resolution of GIMs is considerably coarser than that of SAR images, the GIMs can still be exploited to correct for InSAR ionospheric phase because the ionospheric phase is typically dominated by long-wavelength components (Marconato et al. 2025). Recently, the European Space Agency (ESA) has also begun to include GIM-derived ionospheric corrections in its Extended Timing Annotation

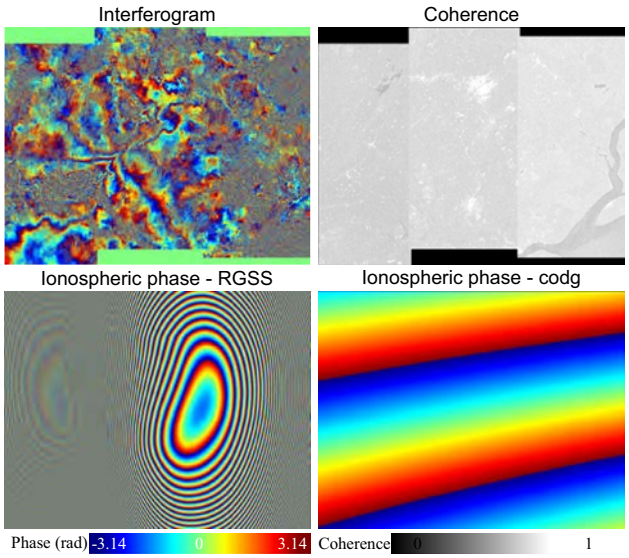

Fig. 1 An example of failed ionospheric phase estimation using the range split-spectrum method for C-band InSAR data. The dense fringes in the estimated ionospheric phase result from unwrapping errors in the sub-band interferograms. In contrast, the ionospheric phase derived from codg GIM is much more accurate. 'RGSS' denotes the range split-spectrum method. The example is from pair 20151216–20160109, frame 1182, path 69 acquired by Sentinel-1 in Sumatra Island, Indonesia

Dataset (ETAD) products released along with Sentinel-1 data (Gisinger et al. 2022). Of particular relevance to this study, the Jet Propulsion Laboratory (JPL) has developed a new GIM product, designated jpld, featuring enhanced temporal and spatial resolution (Mannucci et al. 1999; Martire et al. 2024). When using GIMs for InSAR correction, uncertainties arise from three primary sources: inherent errors in the GIMs themselves, their limited spatial and temporal resolution, and the different signal paths of GNSS and SAR satellites. To date, the impact of these uncertainties on InSAR performance remains poorly characterized, motivating the comprehensive evaluation presented in this study.

In this study, we process approximately one solar cycle (2014–2023) of C-band Sentinel-1 data acquired along very long tracks (more than 1500 km) over two representative regions: a geomagnetic low-latitude area in northern Chile, characterized by high ionospheric activity, and a geomagnetic midlatitude area on the Tibetan Plateau, characterized by low ionospheric activity. Both areas exhibit high interferometric coherence, enabling us to apply the range split-spectrum method to generate high-precision estimates of the ionospheric phases, which can serve as a reference for evaluating GIM-based corrections. We evaluate the ionospheric correction performance of nine available GIMs (comprising eight IGS GIMs and jpld), as well as ESA's ETAD products. This evaluation is conducted for both individual interferograms and InSAR time series, with time

series results validated against Continuous Global Positioning System (CGPS) station measurements. In addition, we investigate the impact of the scaling factor on the ionospheric correction in InSAR time series, and propose an empirical adaptive scaling factor to improve accuracy. Finally, we analyze the role of the time span in InSAR time series relative to the 11-year solar cycle.

2 Data

2.1 SAR data

This study uses Sentinel-1 TOPS (Terrain Observation by Progressive Scans) mode SAR data. Ionospheric effects depend on both the region and time. The data cover two areas with one geomagnetic low-latitude area in northern Chile, and another midlatitude area on the Tibetan Plateau. They are two representative areas with high and low ionospheric activities. Both areas are tectonically active and have attracted considerable interest in the geoscience community. Chile lies within a subduction zone where the Nazca and Antarctic plates move beneath the South American plate (DeMets et al. 1990; Angermann et al. 1999; Contreras-Reyes et al. 2012), a setting responsible for some of the world's largest earthquakes and volcanic eruptions (Lomnitz et al. 1970; Kelleher et al. 1972). The Tibetan Plateau, in contrast, results from the collision between Indian and Eurasian plates, leading to a diverse range of interesting geoscience phenomena, such as large-magnitude earthquakes (Dewey and Burke 1973; Molnar and Tapponnier 1978; Molnar and Chen 1983). Over the past few decades, InSAR-derived crustal deformation measurements have contributed significantly to understanding the tectonics of both regions (Peltzer et al. 1999; Pritchard et al. 2002; Chlieh et al. 2004; Pritchard and Simons 2004; Wright et al. 2004; Elliott et al. 2010; Delouis et al. 2010).

The Sentinel-1 satellites are in a dawn-dusk, sun-synchronous orbit. For ascending tracks, the local acquisition time is near dusk, when ionospheric activity is typically more pronounced. Conversely, for descending tracks, acquisitions occur near dawn, when ionospheric effects are generally weaker. To ensure a comprehensive assessment, we process data from both ascending and descending tracks in each region.

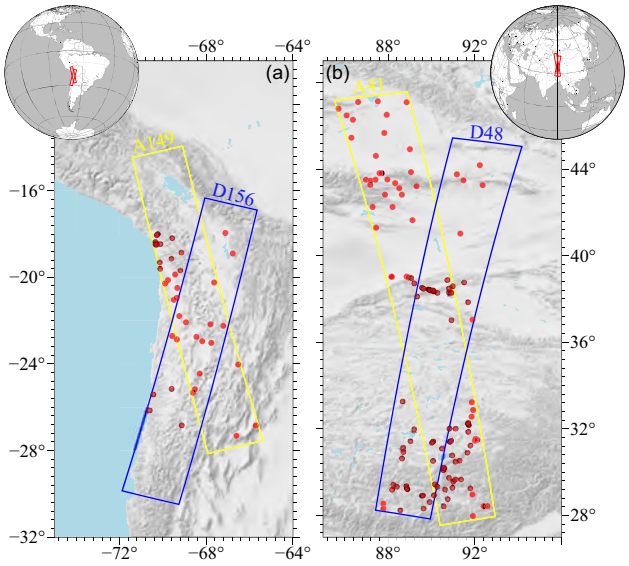

Fig. 2 Coverage of Sentinel-1 SAR data. **a** Tracks A149 and D156 in northern Chile. **b** Tracks A41 and D48 on the Tibetan Plateau. Red dots denote the CGPS stations used to validate InSAR measurements

Table 1 provides the details of the Sentinel-1 TOPS mode SAR data used. Over a long time scale, the data span approximately one solar cycle (2014–2023), enabling investigation of ionospheric effects during different periods in the solar cycle. In addition, the acquisition times of these SAR data closely match the epoches of all GIMs, except for track A149 in northern Chile. This leads to much smaller temporal interpolation errors when aligning GIM epochs with SAR acquisition times. In terms of spatial coverage, the data have very large spatial extents (more than 9 slices, > 1500 km), as shown in Fig. 2, because the InSAR ionospheric phase is

Table 1 Sentinel-1 TOPS mode SAR data used

Area	Northern Chile		Tibetan Plateau			
Track	A149	D156	A41	D48	A12	D121
Number of slices	9–10	9–10	13–14	11–12	6–7	7–8
Acquisition Time (UTC)	23:07	10:01	11:59	00:01	12:15	00:10
Start date	20141027	20150426	20150512	20170326	20150721	20170413
End date	20230326	20230327	20231208	20231126	20230317	20231120
Reference date	20150811	20150426	20170218	20170326	20150721	20170413
Number of dates	160	191	225	167	197	190
Number of dates excluded	4	5	1	3	2	5

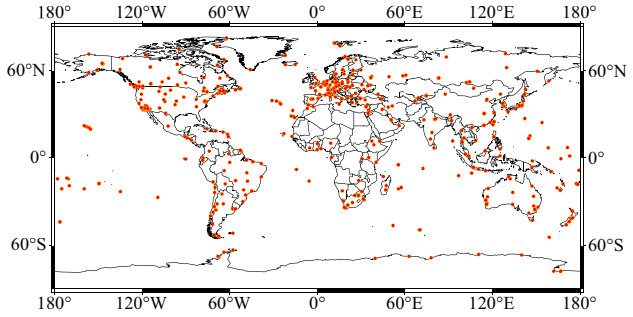

Fig. 3 IGS permanent network of stations

dominated by long-wavelength components. These regions are arid, and the coherence remains high throughout the observation period. The high coherence is a prerequisite for obtaining high-precision estimates of the ionospheric phase using the range split-spectrum method. Additionally, we have processed two more tracks with smaller spatial extents (A12 and D121, ~ 6 slices, ~ 1200 km) on the Tibetan Plateau (Fig. S1 in the supplementary information) to supplement our analysis.

Not all SAR acquisitions were retained for analysis. Some acquisition dates are discarded due to missing slices, lower-quality orbit data labeled as "DEGRADED-MANOEUVRE" (Peter et al. 2021), and the swath starting range problem in range split-spectrum processing (Liang et al. 2019). The numbers of remaining dates are listed in the penultimate row in Table 1. We further exclude dates for which one or more GIMs are unavailable, as shown in the last row of Table 1.

2.2 IGS GIMs

The ionosphere is a dispersive medium, and its effects on microwave signals are inversely proportional to signal frequency. Leveraging this property, GIMs are generated by combining multi-frequency GNSS observations and mapping the resulting slant TEC to vertical TEC. Since 1998, the IGS ionosphere working group has been routinely generating GIMs, by exploiting its permanent global network of more than 500 GNSS stations as shown in Fig. 3. The observations are independently processed by eight IGS Ionosphere Associate Analysis Centers (IAACs) including the Jet Propulsion Laboratory (JPL) in the USA, the Center for Orbit Determination in Europe (CODE) in Switzerland, the European Space Agency and European Space Operations Center (ESA/ESOC) in Germany, Natural Resources Canada (NRCan) in Canada, the Polytechnic University of Catalonia (UPC) in Spain, the Chinese Academy of Sciences (CAS) in China, Wuhan University (WHU) in China, and the Deutsches Geodätisches Forschungsinstitut-Technische Universität München (DGFI-TUM) in Germany.

The characteristics of the IGS GIMs generated by the IAACs are summarized in Table 2. These GIMs are generated using different interpolation methods from direct TEC estimates derived from GNSS observations. CODE, ESA/ESOC, and NRCan use spherical harmonic expansions (Schaer 1999; Feltens 2007; Ghoddousi-Fard et al. 2011). JPL employs the bicubic spline interpolation (Mannucci et al. 1998). UPC applies a two-layer tomographic model with spline interpolation (Hernández-Pajares et al. 1999). An improved version using Kriging interpolation has also been developed (Orús et al. 2005). CAS generates GIMs by combining generalized trigonometric series functions with spherical harmonics at both local and global scales (Li et al. 2015). WHU uses spherical harmonics and non-negative inequality-constrained least squares (Zhang et al. 2013). DGFI-TUM applies a two-step B-spline function in a Kalman filter (Erdogan et al. 2017; Goss et al. 2020). Additionally,

Table 2 Characteristics of IGS GIMs

GIM	Institution	Base Radius (km)	Iono. Hgt (km)	Temp. Reso. (h/min)	Spat. Reso. (lat × long, deg)	Latency (day/yr)	Available Period
jplg	JPL	6371.0	450	2 h	2.5 × 5	~11 days	19980828-present
codg	CODE	6371.0	450	1 h	2.5 × 5	~11 days	19980601-present
esag	ESA/ESOC	6371.0	450	2 h	2.5 × 5	~11 days	19980601-present
igsg	UWM	6371.0	450	2 h	2.5 × 5	~11 days	19980601-present
emrg	NRCan	6371.0	450	1 h	2.5 × 5	~11 days	19980601-present
upcg	UPC	6371.0	450	2 h	2.5 × 5	~11 days	19980601-present
uqrg	UPC	6371.0	450	15 min	2.5 × 5	~11 days	19980602-present
casg	CAS	6371.0/6371.4	450	2 h/30 min	2.5 × 5	~11 days	19980531-present
whug	WHU	6371.0	450	2 h	2.5 × 5	~11 days	19980531-20210308
otlg	DGFI-TUM	–	450	10 min	2.5 × 5	~11 days	–
jpld	JPL	6371.0	450	15 min	1 × 1	0.5~1 yr	20030101-20250531

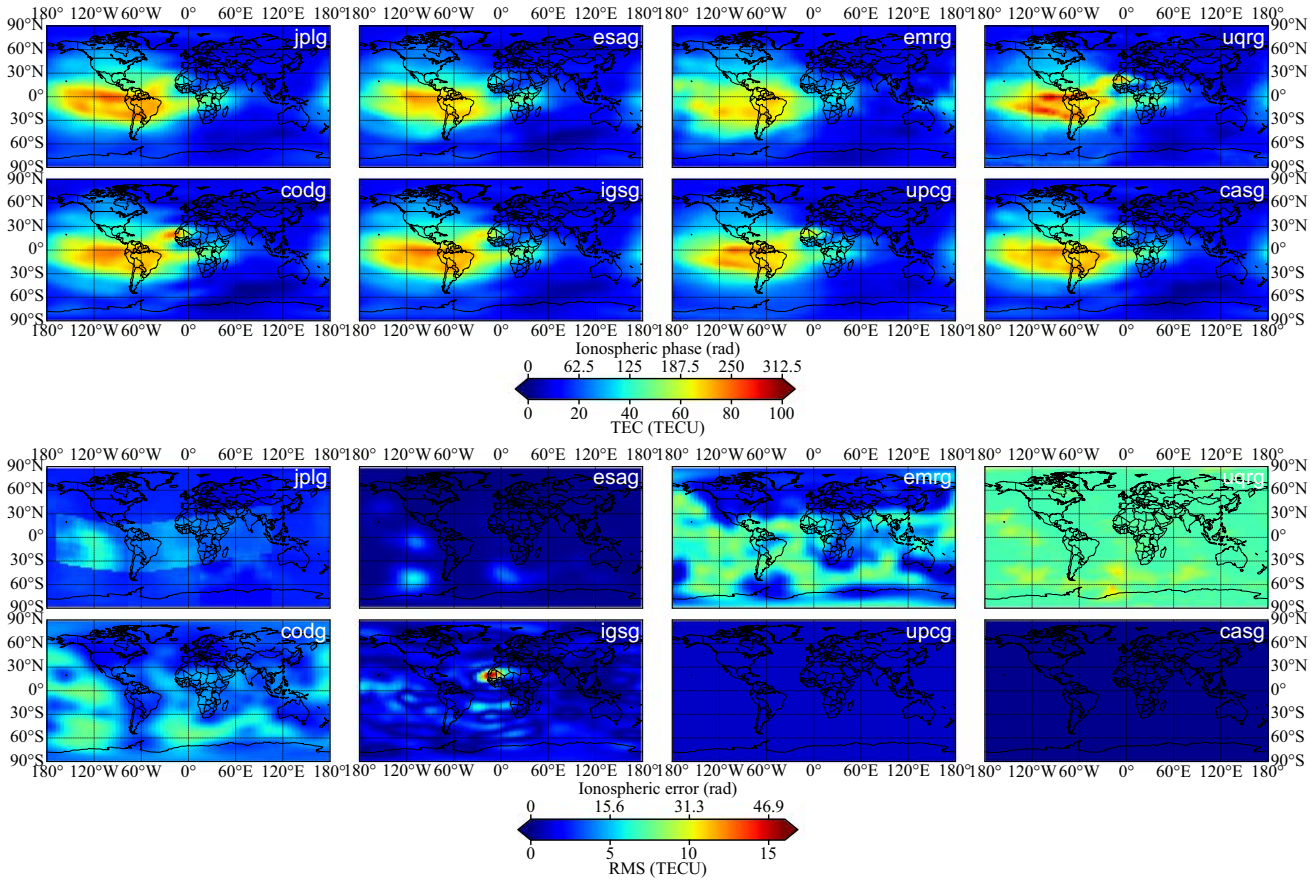

Fig. 4 IGS GIMs and their corresponding RMS maps at 20:00:00 UTC on 22 October 2015 from different IAACs

the University of Warmia-Mazury (UWM) provides combined GIMs as a simple weighted mean of the available GIMs (Hernández-Pajares et al. 2009; Hu et al. 2020).

GIMs provide VTEC expressed in TECU (1 TECU = 10^{16}electrons/m^2). They are available as rapid, final and predicted products, which differ in latency and accuracy, depending on the quality of the GNSS orbit and clock data used. Rapid solutions are available within 24 h, and final solutions are released with a latency of approximately 11 days, while predicted solutions are generated 1–2 days in advance for forecast purposes. We only use the final products, as they are generated using the most accurate GNSS orbit and clock data. All IGS GIMs adopt the same ionospheric model assumption: The ionosphere is represented as a thin spherical shell at an altitude of 450 km. The standard spatial resolution is 2.5 × 5 degrees (latitude × longitude), while the temporal resolution ranges from 10 min to 2 h depending on the products. casg GIMs feature two possible temporal resolutions and use two possible base radii. whug GIMs are not available since 2021. otlg GIMs are not available by the time of our evaluation. Therefore, whug and otlg are not evaluated. For track D156 in northern Chile, emrg is not available on 20150426, which is selected as the reference date of the InSAR stack, and thus it is not evaluated for this track.

The IGS GIMs have associated uncertainties, which are provided as part of each IAAC's release. An example is shown in Fig. 4. To better interpret these uncertainties in the context of InSAR, a 1 TECU error corresponds to a two-way InSAR ionospheric phase error of 3.12 rad, or about π rad, at the center frequency of Sentinel-1. The low spatial and temporal resolution of the IGS GIMs is another source of uncertainty. In addition, the true height of maximum electron density can be different from the height of the spherical shell (450 km), which also causes errors in the correction. These combined sources of uncertainty motivate the comprehensive evaluation of the IGS GIMs for InSAR ionospheric correction presented in this study.

2.3 JPL high-resolution GIM

In addition to the standard IGS products, JPL has been producing jpld GIMs using a three-shell model (Mannucci et al. 1998, 1999) since January 2003. jpld GIMs are released with a latency of approximately six months to one year. jpld

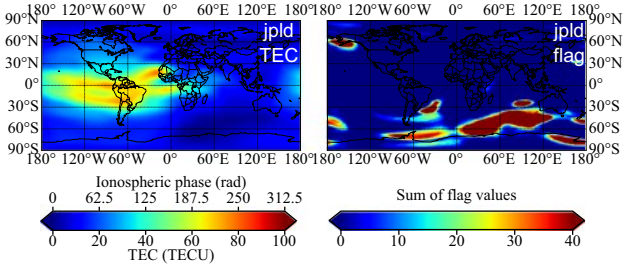

Fig. 5 jpld GIM at 20:00:00 UTC on 22 October 2015 (left), and the sum of flag values of all TEC maps in October 2015 (right)

GIMs offer substantially higher spatial and temporal resolution than conventional IGS GIMs: a temporal sampling of 15 min and a spatial grid of 1° × 1° in latitude and longitude. This improved spatial and temporal resolution makes jpld potentially suitable for InSAR ionospheric correction. jpld GIMs are generated as part of the daily operational GIM processing for the Deep Space Network (DSN). The underlying processing incorporates observations from multiple GNSS constellations: GPS and GLONASS were used from 1 January 2003 to 6 July 2021, and GPS and Galileo have been used thereafter. The algorithm occasionally produces negative TEC values. In such cases, the values are set to a minimum of 0.1 TECU, and a corresponding data quality flag is provided to identify these instances. Unlike the IGS GIMs, which are distributed in IONEX format, jpld GIMs are provided in NetCDF4 format, which includes a dedicated layer for the data quality flag, as shown in Fig. 5. For several days in January 2023, the temporal coverage of the jpld GIM is limited to 00:00 UTC to 23:30 UTC[1].

JPL also generates Near-Real-Time Global Ionospheric Maps (NRTGIM) at a resolution of 15 min (temporal) and 1° × 1° (spatial) through its GUARDIAN (GNSS-based Upper Atmospheric Realtime Disaster Information and Alert Network) system since September 2022; however, they are not used in this study.

2.4 ETAD products

Since July 21, 2023, ESA has been providing the ETAD products alongside Sentinel-1 data. These products, distributed in NetCDF format, provide multiple correction layers designed to correct Sentinel-1 Single Look Complex (SLC) products acquired in Interferometric Wide swath (IW) and Stripmap (SM) modes (Gisinger et al. 2022, 2023). For each burst, the ETAD product consists of 14 layers, including two 1D time (range and azimuth times) layers, three 2D WGS-84 coordinates (longitude, latitude, and height) layers, and nine 2D correction layers. The uncertainties of the correction layers vary. The errors associated with SAR focusing can be precisely calculated. The solid Earth tides can also be precisely calculated using existing models. The tropospheric corrections based on Numerical Weather Prediction (NWP) data from European Centre for Medium-Range Weather Forecasts (ECMWF) have been shown to substantially reduce the tropospheric delays in previous studies (Jolivet et al. 2014; Yu et al. 2018; Cao et al. 2021). The ionospheric correction layer is derived from codg GIMs with a scaling factor of 0.9[2], which is an empirical value adjusted from the analysis of TerraSAR-X (Balss et al. 2018). Unlike the other correction layers, the performance and uncertainties of this ionospheric correction layer when applied to C-band InSAR remain poorly characterized, motivating the evaluation presented in this study.

By the time of our evaluation, only a limited number of ETAD products had been released. The differences between the ionospheric phases from the official ETAD products and those computed from codg GIMs using our processing workflow, which can be considered as improved ETAD products, are sufficiently small to be negligible as demonstrated in Sect. 3.4. Therefore, ionospheric corrections from codg GIMs also serve as a proxy for the official ETAD products in our evaluation.

3 Methods

3.1 Processing of InSAR data

We use the topsStack workflow in the InSAR Scientific Computing Environment version 2 (ISCE2) to process the Sentinel-1 TOPS mode SAR data. topsStack performs routine InSAR stack processing (Fattahi et al. 2017) and implements the range split-spectrum method for the ionospheric phase estimation for InSAR stack (Liang et al. 2019). We use 30 m Shuttle Radar Topography Mission (SRTM) Digital Elevation Model (DEM) (Farr et al. 2007) for geometric coregistration and topographic phase removal. We enable the Enhanced Spectral Diversity (ESD) in coregistering the stack. To construct the interferogram stack, one date is connected with six subsequent dates. Since the ionospheric phase is dominated by long-wavelength signals, the interferograms are multilooked by a large number of looks, with 40 in range and 10 in azimuth (corresponding to a ground resolution of approximately 93.2 m × 141.0 m). This aggressive multilooking reduces computational cost and storage requirements

[1] https://sideshow.jpl.nasa.gov/pub/iono_daily/gim_for_research/jpld/README_jpld_Apr2024.txt

[2] The scaling factor used in the ETAD ionospheric correction layer has been adjusted to 0.78 in version 3.0 of the processor introduced in June 2025 (Gisinger et al. 2025). However, the data in our experiments were acquired before 2025, and hence we still use 0.9 as the ETAD scaling factor in our evaluation.

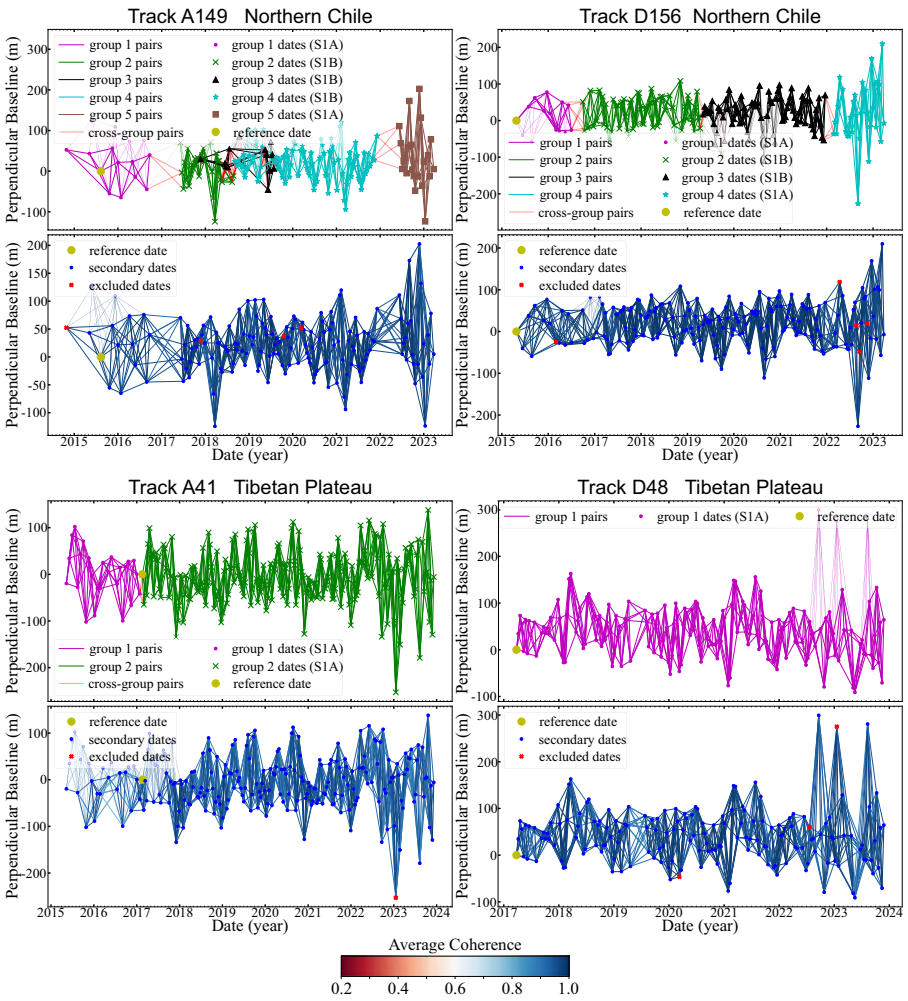

Fig. 6 Networks of InSAR stacks. In each panel, the upper plot shows the ionospheric phase estimation network using the range split-spectrum method, while the lower plot shows the InSAR network for time series analysis. In the lower plots, the acquisitions marked by red crosses are excluded because of missing GIMs. The number of these acquisitions is also listed in Table 1. The colors of the lines connecting the dates denote the coherence of InSAR pairs. The high coherence enables reliable estimation of the ionospheric phase using the range split-spectrum method

while preserving the long-wavelength signals of interest for ionospheric analysis.

3.2 Range split-spectrum method for ionospheric phase estimation

As in GNSS data processing, the range split-spectrum method exploits the frequency dependence of the ionospheric phase by forming interferograms from two distinct sub-bands within the SAR range spectrum (Rosen et al. 2010; Brcic et al. 2010; Gomba et al. 2016). Details of the implementation in topsStack can be found in Liang et al (2019). The method yields precise estimates of the ionospheric phase to serve as a reference, against which we evaluate GIM-based corrections. However, it's challenging to apply this method operationally to C-band SAR data due to its low coherence and phase unwrapping errors. In fact, this method can only reliably estimate the ionospheric phase in C-band interferograms in areas with high coherence, which significantly limits its applicability in C-band InSAR. It is further complicated by the TOPS mode SAR products, whose inaccurate parameters often lead to swath inconsistencies in the estimates. Therefore, special care is required in the processing to secure high-quality estimates.

A known issue in processing Sentinel-1 TOPS mode data for the range split-spectrum analysis arises when the swath starting ranges differ between the two SLC products used to form an interferogram. In such cases, inconsistencies can arise between adjacent swaths in the sub-band interferograms, which is then significantly amplified in the estimated ionospheric phase. Although the swath difference can, in principle, be estimated using the overlap area between adjacent swaths, the estimation precision depends on coherence and may be further significantly degraded by phase unwrapping errors, depending on implementation details. To minimize this problem, we examine the swath starting ranges of all acquisitions and group them according to their starting range values. Data from Sentinel-1A and Sentinel-1B consistently have different starting ranges, and therefore each group contains data from only one satellite. Groups containing fewer than ten acquisitions are discarded. We form the

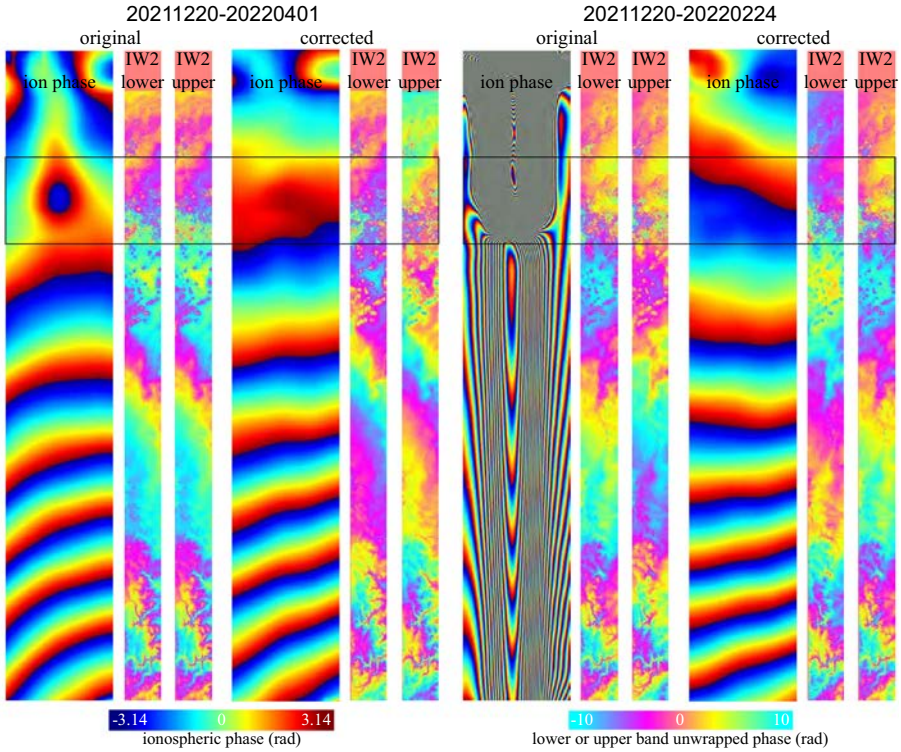

Fig. 7 Correcting swath phase unwrapping errors in cross-group ionospheric phase estimation. Pair 20211220–20220401 exhibits consistent phase unwrapping errors in the lower- and upper-band interferograms of swath2. Pair 20211220–20220224 exhibits different phase unwrapping errors in the lower- and upper-band interferograms of swath2. The examples are taken from track D156 in northern Chile

interferogram network in each group independently by connecting each date to its four subsequent dates. A few dates from two temporally neighboring groups are selected to serve as bridges between the two groups. In each group, we also impose a maximum temporal baseline of one year, as the range split-spectrum method heavily relies on coherence. The final networks are shown in Figs. 6 and S2 in the supplementary information.

An additional artifact of cross-satellite pairs is that the resulting ionospheric phase estimate may exhibit a small range ramp, which can be empirically modeled by a polynomial fitting (see Fig. S3 in the supplementary information). Its origin remains unclear; therefore, the ramp is not removed in our processing.

For multilooking, we apply a two-step strategy. Prior to phase unwrapping, the sub-band interferograms are multilooked by 40 × 10 (range × azimuth) looks. A larger number of looks leads to a higher probability of phase aliasing in the multilooked interferogram. Following phase unwrapping, the sub-band interferograms are further multilooked by 5 × 5 (range × azimuth) looks. The total number of looks is thus 200 × 50 (range × azimuth) looks. This aggressive multilooking is justified by the long-wavelength nature of ionospheric phase. For cross-group pairs with different swath starting ranges, the unfiltered ionospheric phase is first estimated independently for each swath. The differences between the unfiltered swath ionospheric phases are estimated using swath overlap areas and are removed prior to swath merging. The ionospheric phase is then strongly filtered by a Gaussian filter with an adaptive window size to suppress the random noise.

The largest source of uncertainty in the final ionospheric phase estimate is phase unwrapping errors, particularly for cross-group pairs where swaths are unwrapped independently. In such cases, a swath may be separated into isolated areas by low coherence areas, and relative phase unwrapping errors occur, which eventually causes large errors in the ionospheric phase estimate. Consequently, manual inspection and correction are required when unwrapping these sub-band interferograms. If one swath is correctly unwrapped, its phase in the overlap area can provide a reference. The relative unwrapping error in an isolated region of the adjacent swath can then be identified and corrected by adding integer multiples of 2π radians to bring the phase into consistency. Figure 7 illustrates two examples of this correction. In the left example of Fig. 7, the phase unwrapping errors of the sub-band interferograms are consistent between the two sub-band interferograms, leading to a much smaller error in the estimated ionospheric phase. In the right example of Fig. 7, the errors differ between the two sub-bands, leading to a much larger error. All these phase unwrapping errors are corrected, as shown in Fig. 7.

Phase unwrapping errors might also occur in same-group pairs, typically in areas affected by decorrelation due to vegetation or sand dunes. If the full-band interferogram in InSAR processing is correctly unwrapped, we can use it to guide the correction of phase unwrapping errors

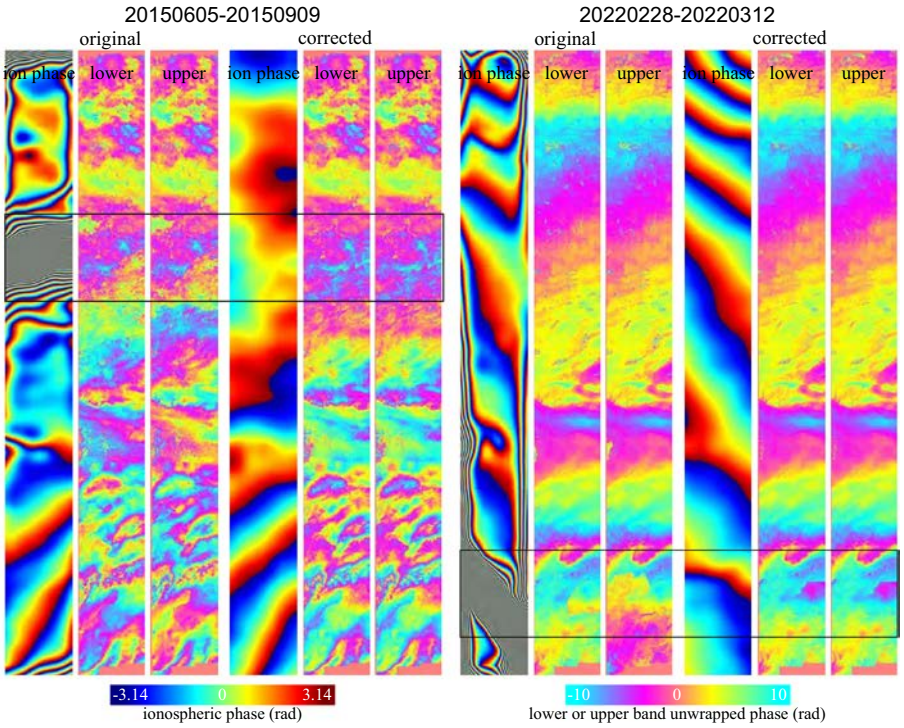

Fig. 8 Correcting phase unwrapping errors in same-group ionospheric phase estimation. The examples are taken are from track A41 on the Tibetan Plateau

in the sub-band interferograms, as their wavelengths are close. The correction method is similar to that of cross-group pairs. Figure 8 presents two correction examples, in which the phase unwrapping errors differ between the two sub-band interferograms, resulting in large errors in the ionospheric phase estimate. A more detailed description of both correction procedures is provided in the supplementary information.

After estimating the ionospheric phase for each pair, we use a least-squares inversion to obtain the ionospheric phase for each date relative to a common reference date. This approach is analogous to standard time series inversion in InSAR.

In addition to the large-scale ionospheric phase, we also estimate the small-scale phase errors caused by the ionosphere in each burst, although these small-scale errors do not have a significant impact on the large-scale analysis.

We use these ionospheric estimates as "true" values to evaluate the performance of GIMs. It should be noted, however, that the range split-spectrum method cannot provide reliable ionospheric phase estimate for C-band InSAR under many landcovers, because of low coherence and phase unwrapping errors. Since only high-coherence areas are selected in this study, the method can generate reliable results. Nevertheless, even in these favorable areas, phase unwrapping errors can occasionally occur, necessitating the manual inspection and correction procedures. These challenges motivate the use of GIMs for the ionospheric correction of C-band InSAR.

3.3 Processing of GIMs

To evaluate GIM-derived ionospheric corrections against those estimated by the range split-spectrum method, the GIMs need to be processed to match the InSAR data both spatially and temporally. The SAR imaging geometry is shown in Fig. 9. The GNSS satellites orbit the Earth at an altitude of approximately 20,000 km, whereas SAR satellites operate at much lower altitudes, typically between 600 and 800 km. The Sentinel-1 orbit altitude is about 698–726 km (Yague-Martinez et al. 2016). The GIMs derived from GNSS observations thus represent all the electrons through the entire ionosphere, but the SAR signal experiences only the electrons below SAR orbit.

We follow the approach for generating the ionospheric correction layer in the ETAD product (Gisinger et al. 2023) to compute the ionospheric phase from GIM for each SAR acquisition. The detailed processing workflow can be found in the supplementary information, including Ionospheric Pierce Point (IPP) position estimation, longitude adjustment, spatiotemporal interpolation, and geometric projection and scaling. We then resample the ionospheric phase images of the secondary dates to the image coordinate of the reference date using the offsets between SAR images estimated during InSAR coregistration.

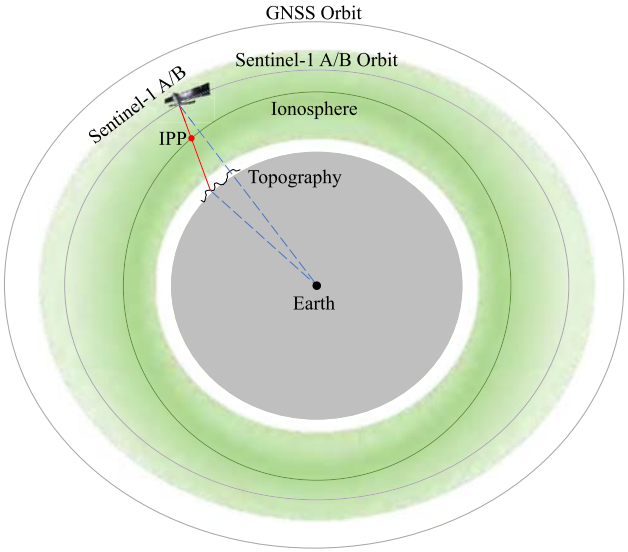

Fig. 9 SAR imaging geometry. The light green layer represents the ionosphere, which is modeled as a thin spherical shell at an altitude of 450 km (the green sphere). The peak of the actual VTEC density profile of the ionosphere varies with both time and location. The gray elliptical circles represent the GNSS orbit (approximately 20,000 km altitude) and the Sentinel-1 A/B orbit (about 700 km altitude), respectively. The figure is not to scale

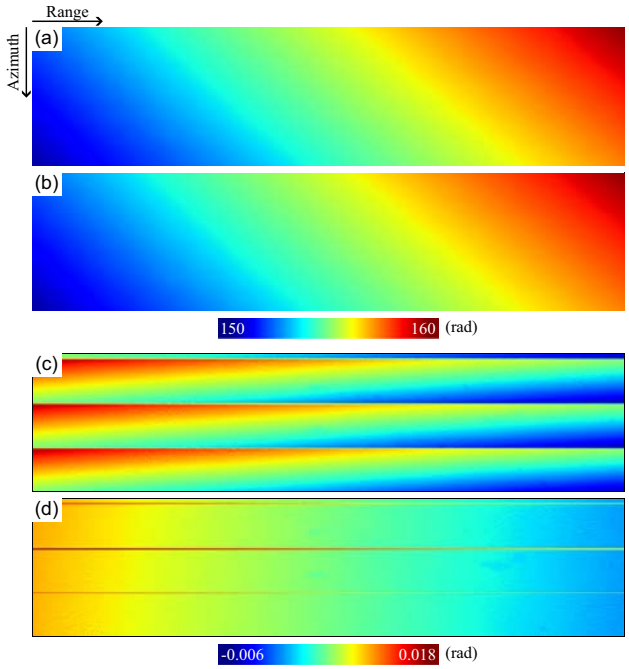

Fig. 10 Comparison between the ETAD product and our result for Burst0027 of swath2 from a slice (S1A_IW_SLC__1SDV_20231019T121613_20231019T121640_050834_06207E_1BA1.SAFE) acquired on track A12 on the Tibetan Plateau on 19 October 2023. **a** ETAD. **b** Our result. **c** Difference. **d** Difference when the ETAD update rate (every second) is adopted

3.4 Comparison with ETAD products

codg GIMs from IGS and a scaling factor of 0.9 are used to compute the ionospheric correction layer in the ETAD products. By the time of our evaluation, only a limited number of ETAD products were available, preventing their use for full time series InSAR ionospheric correction. However, they can be used for comparison with our results.

To enable a direct comparison, we adapt our processing workflow to match that for generating the ETAD products. Therefore, we replace the bicubic interpolation used in our standard GIM processing with the bilinear interpolation used by ETAD when spatially interpolating GIMs. Moreover, we generate the ionospheric phase for each burst, consistent with the ETAD products. The comparison results for one burst are shown in Fig. 10. Some differences are observed in Fig. 10c. These differences arise from an artifact in the ETAD products: The ETAD processing updates the parameters at a rate of once per second instead of for every azimuth line, thereby reducing computational costs. When the same update rate is adopted in our processing, the artifact vanishes and the difference is negligible, as shown in Fig. 10d.

A second artifact of the ETAD product stems from its interpolation method. To spatially interpolate GIMs, ETAD uses a bilinear kernel. This interpolation might not be adequate considering the very coarse spatial resolution of GIMs. To illustrate this effect, Fig. 11 shows a comparison of the

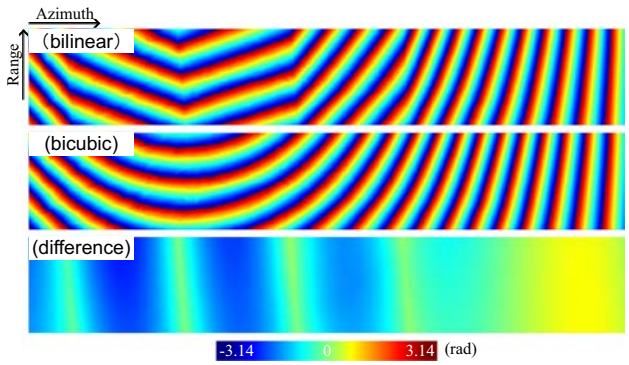

Fig. 11 Comparison between the ionospheric phases generated using bilinear and bicubic interpolation kernels. The resulting artifact of using bilinear interpolation is evident. The results are for pair 20151022–20160102, track A149 in northern Chile. The GIMs used are codg and the scaling factor is 0.9, same as ETAD

two results generated using bilinear and bicubic interpolation kernels.

These comparisons demonstrate that our codg-based results are consistent with the ETAD products, but do not exhibit either of the two artifacts described above. The evaluation of ionospheric correction using our result generated from codg GIMs can thus also represent that using improved ETAD products. Given that the differences between the

ETAD products and the improved ETAD products are very subtle, we therefore do not provide separate evaluation results for the ETAD products.

3.5 InSAR time series analysis

The InSAR stack networks are shown in the lower plot of each panel in Figs. 6 and S2. We exclude dates denoted by red crosses in these figures, for which GIMs are unavailable. We use MintPy (Zhang et al. 2019) to perform InSAR time series analysis and generate both deformation time series and mean velocity fields. After removing the topographic phase, the InSAR phase consists of a variety of components

$$\begin{aligned}\varphi_{\mathrm{InSAR}} &= \varphi_{\mathrm{atm}} + \varphi_{\mathrm{motion}} + \varphi_{\mathrm{physical_process}} + \varphi_{\mathrm{error}} \\ &= \left(\varphi_{\mathrm{tropo}} + \varphi_{\mathrm{iono}}\right) \\ &\quad + \Big(\varphi_{\mathrm{defo}} + \varphi_{\mathrm{plate}} + \varphi_{\mathrm{solid}} + \varphi_{\mathrm{ocean}} \\ &\quad + \varphi_{\mathrm{pole}} + \varphi_{\mathrm{ocean_pole}} + \varphi_{\mathrm{atmospheric}} + \varphi_{\mathrm{non_tidal}}\Big) \\ &\quad + \left(\varphi_{\mathrm{physical_process}}\right) \\ &\quad + \left(\varphi_{\mathrm{DEM_error}} + \varphi_{\mathrm{unwrap_error}} + \varphi_{\mathrm{noise}}\right) \end{aligned} \quad (1)$$

where φ_{atm} is the atmospheric phase including the tropospheric phase delay φ_{tropo} and the ionospheric phase advance φ_{iono}, $\varphi_{\mathrm{motion}}$ is the Earth's surface motion including the phases induced by the ground deformation of interest φ_{defo}, the plate motion φ_{plate}, the solid Earth tide φ_{solid}, the ocean tide loading φ_{ocean}, the pole tide φ_{pole}, the ocean pole tide loading $\varphi_{\mathrm{ocean_pole}}$, the atmospheric tide loading $\varphi_{\mathrm{atmospheric}}$, and the non-tidal loadings $\varphi_{\mathrm{non_tidal}}$, such as the atmospheric and hydrological loadings, $\varphi_{\mathrm{physical_process}}$ is the phase associated with the Earth's surface and near-surface processes other than motions, and φ_{error} is the phase errors including those caused by the DEM error $\varphi_{\mathrm{DEM_error}}$, the phase unwrapping error $\varphi_{\mathrm{unwrap_error}}$ and the decorrelation φ_{noise}.

We remove the tropospheric phase using PyAPS (Jolivet et al. 2014) with the ERA5 products (the fifth generation ECMWF atmospheric reanalysis of the global climate) from ECMWF. The motion induced by the solid Earth tide is removed using PySolid (Zhang et al. 2022; Milbert 2018). Other tidal and loading effects are not removed, as their impacts are sufficiently small to be negligible. For non-tidal loadings, the corresponding models are less accurate; therefore, they are not removed either. The plate motion (Stephenson et al. 2022) is treated as a signal of interest and is not removed from the results. We estimate and remove the phase errors caused by the DEM errors (Fattahi and Amelung 2013) and the phase unwrapping errors (Zhang et al. 2019). Another error source is the phase associated with the Earth's surface and near-surface processes other than motions. A typical example of such an error is the non-zero closure phase (Ansari et al. 2021; Zheng et al. 2022), but no robust and generally applicable methods are currently available for its correction.

Table 3 Corrections applied to CGPS measurements

Correction Term	Northern Chile (NGL)	Tibetan Plateau (Wang and Shen 2020)
Ionosphere	Applied	Applied
Troposphere	Applied	Applied
Plate motion	Not applied	Applied/Not applied
Solid Earth tide	Applied	Applied
Ocean tide	Applied	Applied
Pole tide	Applied	Applied

We use CGPS measurements to validate the InSAR results. For northern Chile, the CGPS measurements released by Nevada Geodetic Laboratory (NGL) (Blewitt 2024) are used. Stations with poor data quality or located in areas affected by large transient deformations (e.g., coseismic or postseismic signals) are excluded from the analysis. For the remaining stations, only high-quality daily records are used to estimate the mean velocities. Finally, the CGPS mean velocities are projected into radar Line-Of-Sight (LOS) directions. For Tibetan Plateau, however, raw CGPS time series are not available. Instead, published velocities from Wang and Shen (2020) are used. The CGPS measurements in the vertical (up) direction are typically with lower precision, and long-wavelength motions in this direction are generally small. Therefore, we only use the east and north components of CGPS measurements. The various corrections applied in these CGPS measurements are summarized in Table 3. For the CGPS velocities of Tibetan Plateau, we use the results without removing plate motion.

4 Performance of GIMs

4.1 Performance of GIMs in the ionospheric correction of individual interferograms

The performance of GIMs varies in correcting individual interferograms for the ionospheric phase. We compare the ionospheric phase derived from GIMs with that estimated by the range split-spectrum method, which is considered as the reference or "true" ionospheric phase. The scaling factor in Eq. (S7) is set to 0.9, consistent with the value used in the ETAD products. Because it is difficult to define a quantitative metric for directly evaluating the uncertainty of ionospheric corrections, we adopt a qualitative classification scheme, which is applied consistently to all tracks and all GIMs. The ionospheric phases derived from GIMs are classified into three quality levels based on the following criteria:

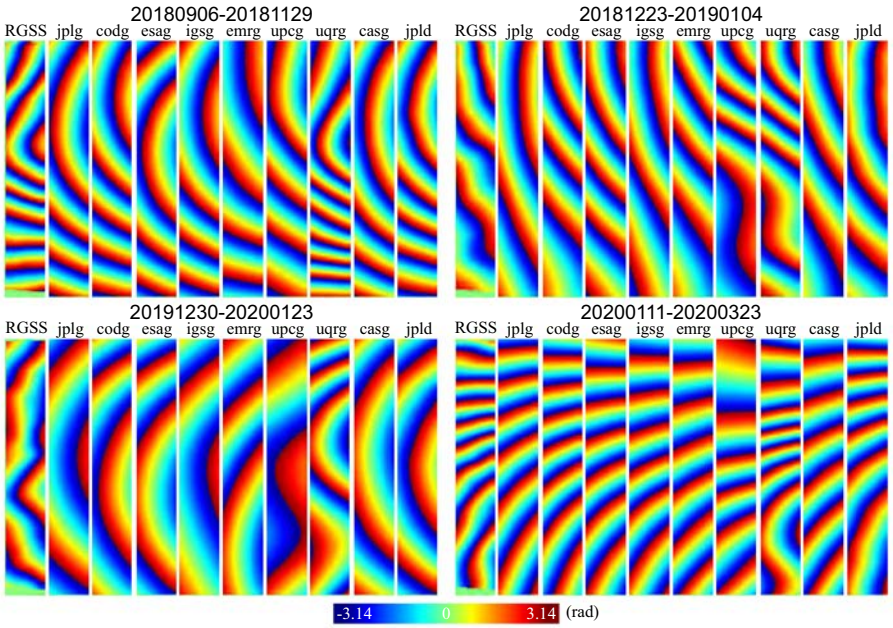

Fig. 12 Examples of the ionospheric phase derived from GIMs. Results from the range split-spectrum method are considered as "true" ionospheric phase. The results are for track A149 in northern Chile. The scaling factor used for GIMs is 0.9

Table 4 Proportions of high-, moderate-, and low-quality ionospheric estimates derived from GIMs for individual interferograms across all tracks (scaling factor = 0.9)

GIM	High-quality	Moderate-quality	Low-quality
jplg	6.50%	64.75%	28.75%
codg	6.00%	64.42%	29.58%
esag	4.25%	61.08%	34.67%
igsg	4.33%	62.17%	33.50%
emrg	2.00%	53.20%	44.80%
upcg	3.08%	53.92%	43.00%
uqrg	3.50%	42.00%	54.50%
casg	3.25%	58.00%	38.75%
jpld	9.75%	59.92%	30.33%

0% 100%

(1) High quality: The ionospheric phase derived from GIMs closely matches the reference ionospheric phase in terms of both the number of fringes and the trend of the fringes.
(2) Moderate quality: The ionospheric phase derived from GIMs captures the overall trend of the fringes but differs in the number of fringes.
(3) Low quality: The ionospheric phase derived from GIMs shows little similarity to the reference ionospheric phase, even in the broad fringe trend.

Given the inherent subjectivity of the criteria, we present selected examples from track A149 in Fig. 12 to further illustrate the classification criteria (In all figures and tables, 'RGSS' denotes the range split-spectrum method). This track is subject to heavy ionospheric disturbances, since the SAR data are acquired in a low-latitude region at dusk. Although the results derived from different GIMs are broadly similar, they exhibit notable differences in detail. In these examples, the estimate from uqrg for pair 20180906-20181129, the estimates from emrg and casg for pair 20181223-20190104 and the estimate from jpld for pair 20191230-20200123 are considered as high-quality results. The estimates from emrg for pairs 20180906-20181129 and 20191230-20200123, and the estimates from upcg and uqrg for pairs 20181223-20190104, 20191230-20200123 and 20200111-20200323 are considered as low-quality results. The remaining ones in Fig. 12 are considered as moderate-quality results.

There are more than 800 interferograms for each track, making a complete manual classification impractical. Therefore, we randomly select 200 interferograms per track for statistical analysis. The proportions of the three quality levels for each track are summarized in Tables S1–S6 in the supplementary information and in Table 4. The results reveal that moderate-quality results are most prevalent, with a significant number of low-quality results also observed. Ascending tracks exhibit a higher proportion of moderate-quality results than descending tracks. We attribute this to the smaller ionospheric phase magnitudes on descending tracks (due to the acquisition time near dawn), which makes the GIM errors more pronounced. In addition, GIMs exhibit poor performance for track A149 compared to other ascending tracks. This is likely due to two factors: The IGS stations are distributed sparsely over oceanic regions; the acquisition time differs from the nominal epochs of most IGS GIMs by a substantially larger temporal mismatch than for other tracks.

Among these GIMs, jpld exhibits the best performance, followed by jplg and codg. The better performance of jpld likely stems from its much higher temporal and spatial resolutions. Among the IGS GIMs, uqrg shows the poorest

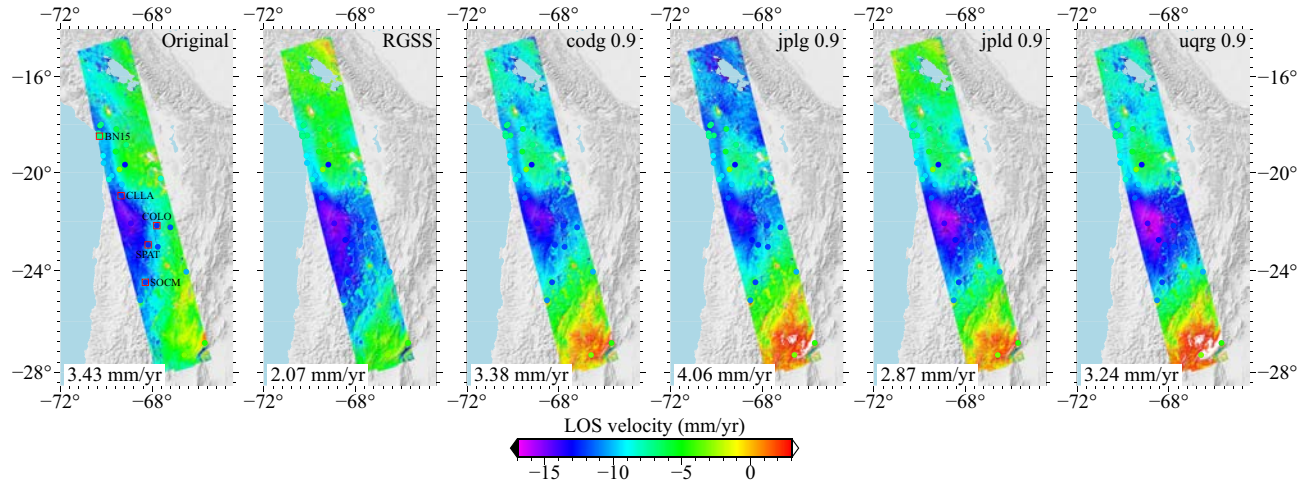

Fig. 13 Mean deformation velocities of track A149 in northern Chile, with and without ionospheric corrections. A scaling factor of 0.9 is used for the correction with GIMs. The circles represent the locations of CGPS stations, with colors denoting mean velocity measured by CGPS projected into the InSAR LOS direction. The stations used in Fig. 18 and Fig. S15 are marked with red squares and are labeled with their corresponding station names in the first panel

performance, with the exception of track A149 in northern Chile. The exception is likely because of its higher sensitivity to rapid and large ionospheric variations with a higher temporal resolution. For track A149 in northern Chile, codg generally outperforms jplg. We attribute this to the temporal alignment of SAR acquisition and GIM product times. As shown in Tables 1 and 2, the acquisition time of A149 (~ 23:07 UTC) falls approximately midway between two jplg time nodes but coincides closely with a codg time node, thereby reducing temporal interpolation errors for codg in this specific case.

4.2 Performance of GIMs in the ionospheric correction of InSAR time series

We generate the mean deformation velocities and displacement time series from three sets of interferograms: (1) original, (2) corrected using the range split-spectrum method, and (3) corrected using GIM-derived ionospheric phases. For the GIMs-derived corrections, we test two scaling factors in Eq. (S7): 0.9, the one used in the ETAD products (Gisinger et al. 2022) and 0.69 (Zhang et al. 2022). The results obtained with a scaling factor of 0.9 are presented in the main text, while those using 0.69 are provided in the supplementary information. We compare the InSAR results from each correction approach with the CGPS measurements projected into the radar LOS directions. We select the four best-performing GIMs in correcting individual interferograms, including codg, jplg, jpld and uqrg, and evaluate their performances in the ionospheric correction of InSAR time series.

Figures 13 and S6 show the mean deformation velocity fields of track A149 in northern Chile. The ionospheric phase of this track is very strong, as illustrated by the examples shown in Fig. 12. Surprisingly, the original mean velocity shows little evidence of significant ionospheric contamination. The time span of the data (20150507 ~ 20230326, 20141027 is excluded due to unavailable GIMs) is nearly symmetric about the solar minimum between solar cycles 24 and 25 in December 2019. The ionospheric effects are therefore largely averaged out during the linear inversion for mean velocity. We therefore present an additional analysis in Figs. 14 and S7 spanning the second half of solar cycle 24 (20150507-20191124). As expected, the original mean velocity is now strongly affected by the ionosphere. This demonstrates that the impact of the ionospheric phase on mean velocity estimates depends strongly on the time span of the data relative to the solar cycle, which will be further explored in Sect. 5.

The mean deformation velocity fields of other tracks are presented in Figs. 15, 16 and 17 and Figs. S8–S10, with additional results for two more tracks on the Tibetan Plateau shown in Figs. S11–S14. In most cases, GIM-based corrections can improve the mean velocity estimates, with significant improvements observed when the ionospheric phase is strong.

To complement the velocity analysis, we examine the displacement time series of track A149 in northern Chile with and without ionospheric corrections, as shown in Figs. 18 and S15. Because InSAR measurements are relative both temporally and spatially, we use a reference date 20150811, and a reference CGPS station BN15. The reference CGPS station BN15 and the secondary CGPS stations are labeled in the

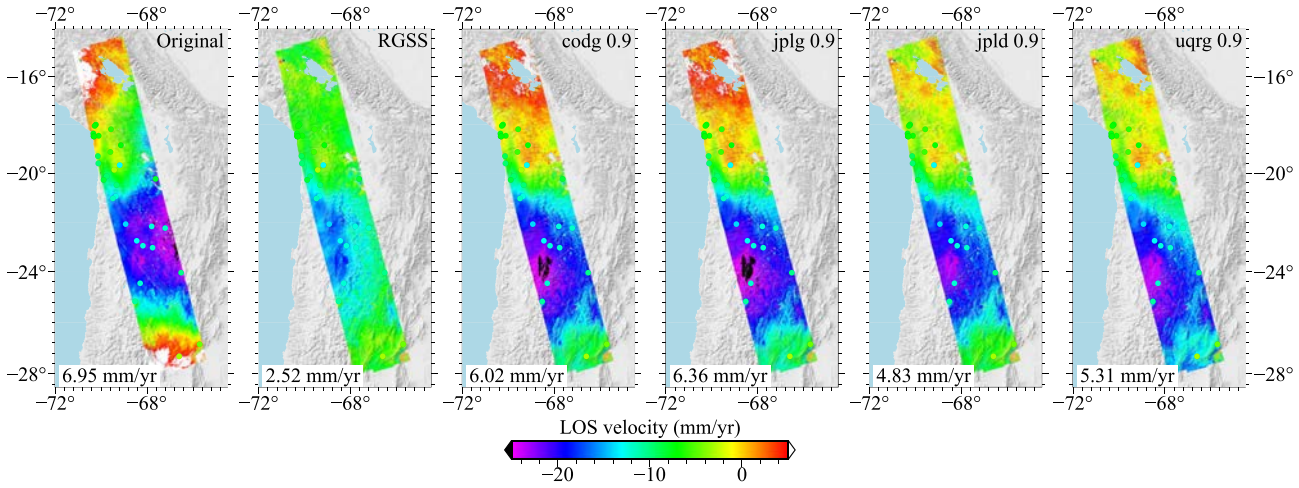

Fig. 14 Mean deformation velocities of track A149 in northern Chile, spanning the second half of solar cycle 24, with and without ionospheric corrections. A scaling factor of 0.9 is used for the correction with GIMs. The circles represent the locations of CGPS stations, with colors denoting mean velocity measured by CGPS projected into the InSAR LOS direction

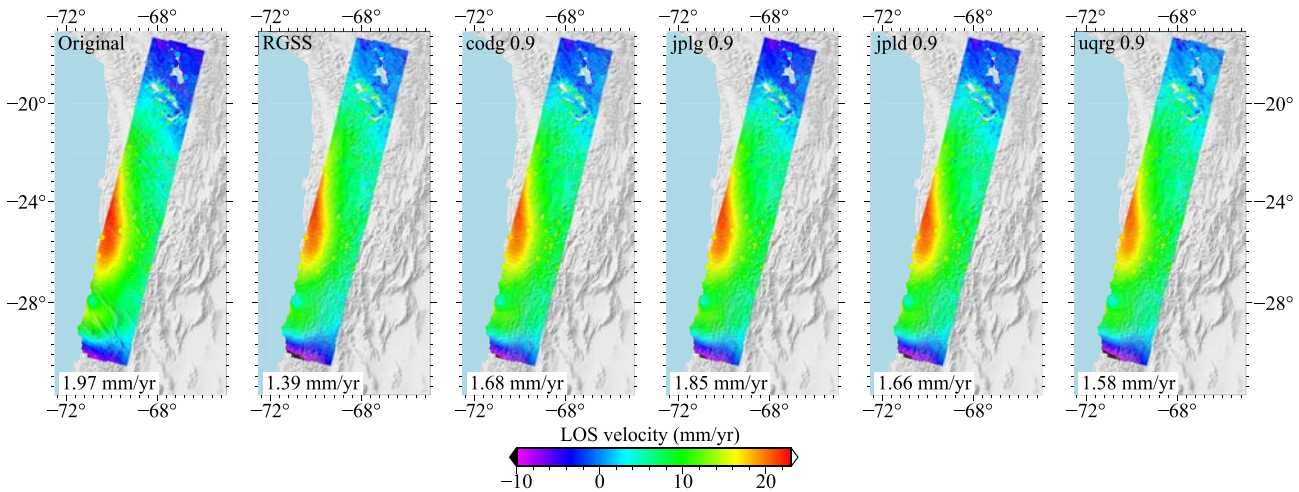

Fig. 15 Mean deformation velocities of track D156 in northern Chile, with and without ionospheric corrections. A scaling factor of 0.9 is used for the correction with GIMs. The circles represent the locations of CGPS stations, with colors denoting mean velocity measured by CGPS projected into the InSAR LOS direction

first panel of Fig. 14. Comparisons between different time series also confirm that GIM-based corrections can reduce ionospheric signals.

The ionospheric effects in northern Chile are strong, particularly for ascending-track data acquired near dusk local time. For track A149 in northern Chile, the IGS GIMs provide limited improvements in the velocity estimates. In contrast, jpld can still achieve a substantial improvement owing to its higher temporal and spatial resolutions. The poor performance of the IGS GIMs on A149 likely stems from multiple factors. First, the region lies adjacent to the ocean, where the sparse distribution of IGS stations degrades GIM accuracy. Second, the ionosphere is highly active at the SAR acquisition times, with rapid spatial variations that exceed the resolving capability of coarse IGS GIM grids. Third, temporal alignment plays a critical role: The acquisition time of A149 (~ 23:00 UTC, see Table 1) falls midway between the two-hourly time nodes of most IGS GIMs, leading to increased interpolation errors. Among the IGS GIMs, uqrg and codg perform relatively better, because their time nodes align more closely with the SAR acquisition times. In general, the scaling factor 0.69 performs better than 0.9, as the errors in the IGS GIMs are suppressed by a smaller scaling factor. For track D156 in northern Chile, however, corrections from all GIMs improve the velocity estimates, as shown in

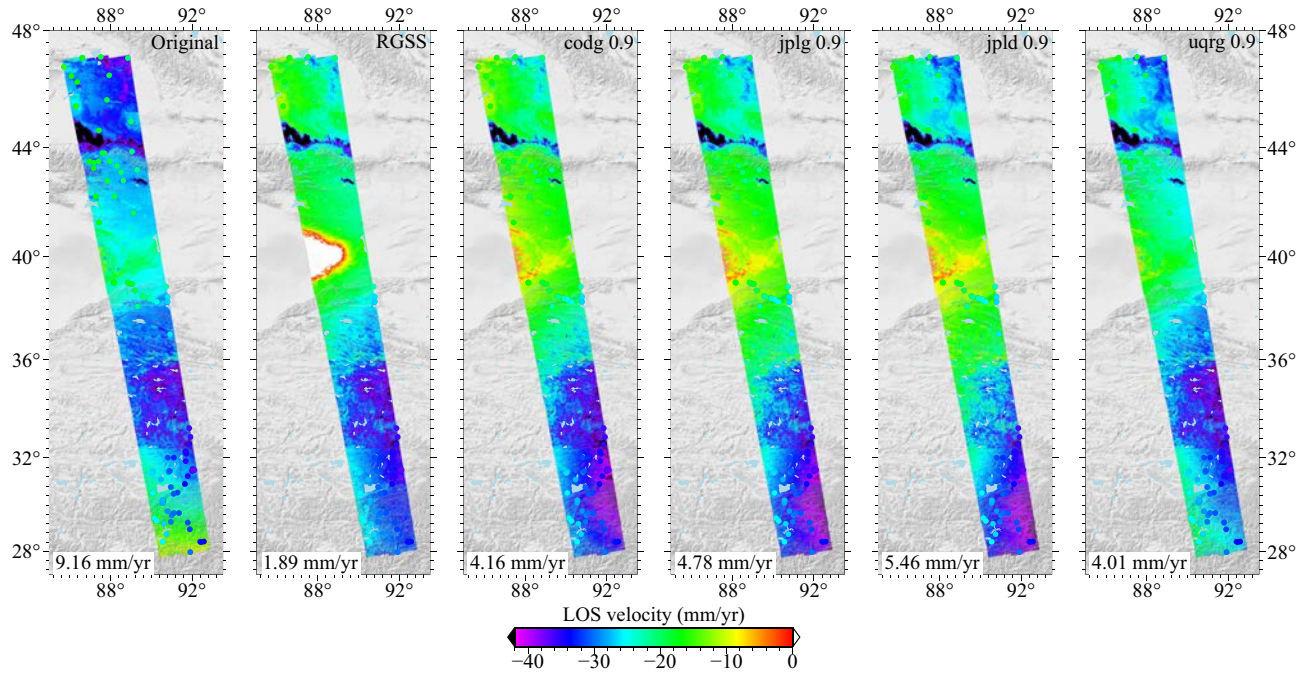

Fig. 16 Mean deformation velocities of track A41 on the Tibetan Plateau, with and without ionospheric corrections. A scaling factor of 0.9 is used for the correction with GIMs. The circles represent the locations of CGPS stations, with colors denoting mean velocity measured by CGPS projected into the InSAR LOS direction

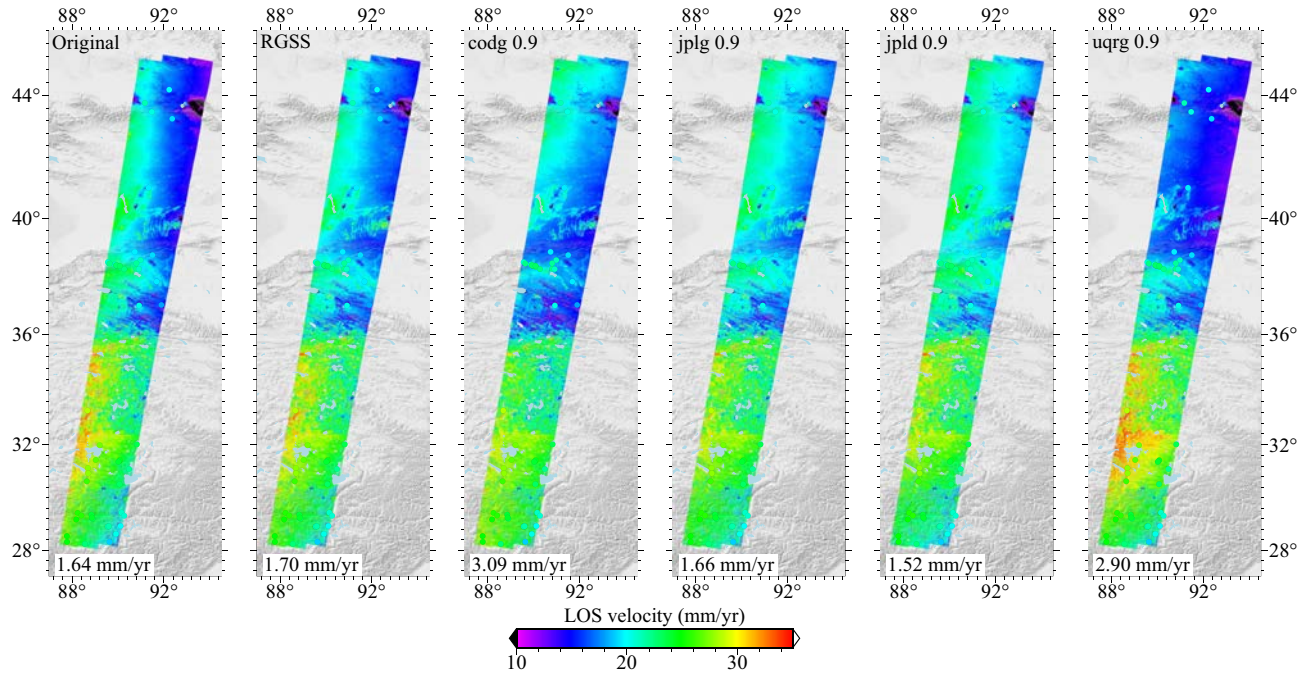

Fig. 17 Mean deformation velocities of track D48 on the Tibetan Plateau, with and without ionospheric corrections. A scaling factor of 0.9 is used for the correction with GIMs. The circles represent the locations of CGPS stations, with colors denoting mean velocity measured by CGPS projected into the InSAR LOS direction

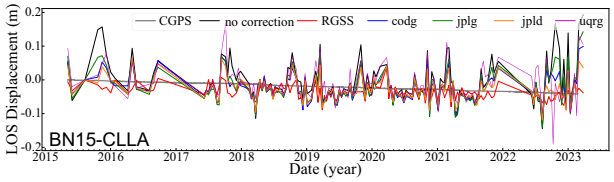

Fig. 18 Deformation time series of track A149 in northern Chile, from CGPS (CLLA) and InSAR with and without ionospheric corrections. A scaling factor of 0.9 is used for the correction with GIMs

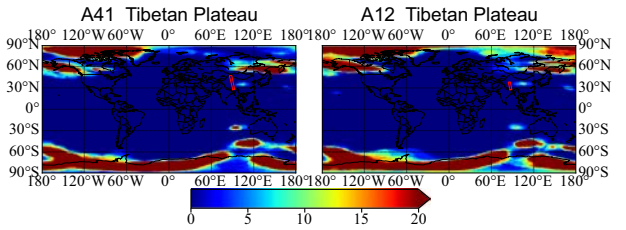

Fig. 19 Cumulative flag values of jpld for tracks A41 and A12 on the Tibetan Plateau around their acquisition times. The red rectangles in the maps denote the SAR footprint

Figs. 15 and S8. In this case, scaling factors 0.69 and 0.9 perform almost equally well. In addition, the SAR acquisition times are very close to the time nodes of all GIMs, thereby leading to very small errors after the temporal interpolation of GIMs. In all cases, jpld improves the velocity estimate. It also demonstrates the best performance among the GIMs. The only exception is that uqrg exhibits a slightly better performance than jpld for track D156.

The ionosphere is generally much less active on the Tibetan Plateau, but on ascending tracks ionospheric effects are still appreciable. For the tracks A41 and A12 on the Tibetan Plateau, large ionospheric effects are observed in original velocity estimates, and all GIMs with scaling factors 0.69 and 0.9 largely remove ionospheric errors in the mean velocities, as shown in Figs. 16, S9, S11, and S12. Notably, the optimal scaling factor varies by GIM: For codg, jplg and jpld, the scaling factor 0.69 yields better performance, while for uqrg, 0.9 is more effective. For descending tracks D48 and D121, the situation is markedly different. Ionospheric signatures are barely detectable in the original velocity fields, as shown in Figs. 17, S10, S13, and S14. In most cases, the errors become larger following GIM corrections, and even if there is improvement, it is marginal. The errors after correction with scaling factor 0.69 are smaller than those with scaling factor 0.9. For these two tracks, even the range split-spectrum method struggles to improve the results, and therefore we do not recommend ionospheric correction for data acquired in regions at midlatitudes on descending tracks. In this region, errors associated with temporal interpolation are not a significant issue, as SAR acquisition times are very close to all GIM product times.

The preceding analyses demonstrate that the performances of different GIMs vary. Among all evaluated GIMs, jpld generally performs much better than the IGS GIMs, improving results in nearly all cases. It even outperforms the range split-spectrum method for track D48 on the Tibetan Plateau. The only exception is track D121, for which the ionospheric phase is small; therefore, applying the jpld correction slightly degrades the results.

Among the IGS GIMs, codg exhibits the most stable and best overall performance, followed by jplg. Previous studies conclude that uqrg generally achieves best performance in VTEC estimation (Chen et al. 2023; Hernández-Pajares et al. 2017). For InSAR ionospheric correction, uqrg sometimes exhibits better performance especially in northern Chile tracks, but overall, its performance is not stable. This may be attributed to its relatively high temporal resolution while using the same original IGS observation data as other IGS GIMs, making it more suitable for regions experiencing rapid ionospheric variations.

For tracks A41 and A12, however, jpld performs slightly worse than some IGS GIMs. Figure 19 displays the cumulative flag values of jpld over the periods used for ionospheric correction. Flag value 1, indicating artificially assigned TEC values (see Sect. 2.3), appears near the Tibetan Plateau after 2021. The imprecise TEC measurements around these two tracks might have degraded the performance of jpld. Several observations support this hypothesis:

(1) In Figs. 16, S9, and Figs. S11–S12, areas adjacent to regions with high flag value regions exhibit worse results when using jpld correction.
(2) In Tables S14 and S16, the Root-Mean-Square (RMS) errors with jpld corrections using an empirical adaptive scaling factor for the pre-2021 period are consistently smaller than other methods, but become less stable post-2021.

4.3 Scaling factor

In previous studies (e.g., Gisinger et al. 2022; Zhang et al. 2022; Marconato et al. 2025), a fixed scaling factor was commonly applied for ionospheric correction. The early ETAD products adopted a scaling factor of 0.9 (Gisinger et al. 2022), while a smaller value of 0.69 is suggested in (Zhang et al. 2022). Neither of the two scaling factors performs consistently better across all cases. To investigate whether an optimal fixed factor exists, we perform InSAR time series analysis using GIM-based corrections with scaling factors ranging from 0.5 to 1.0. For each factor, we compare the resulting mean velocities with CGPS measurements. The results are shown in Table 5 and Tables S7–S11. These results

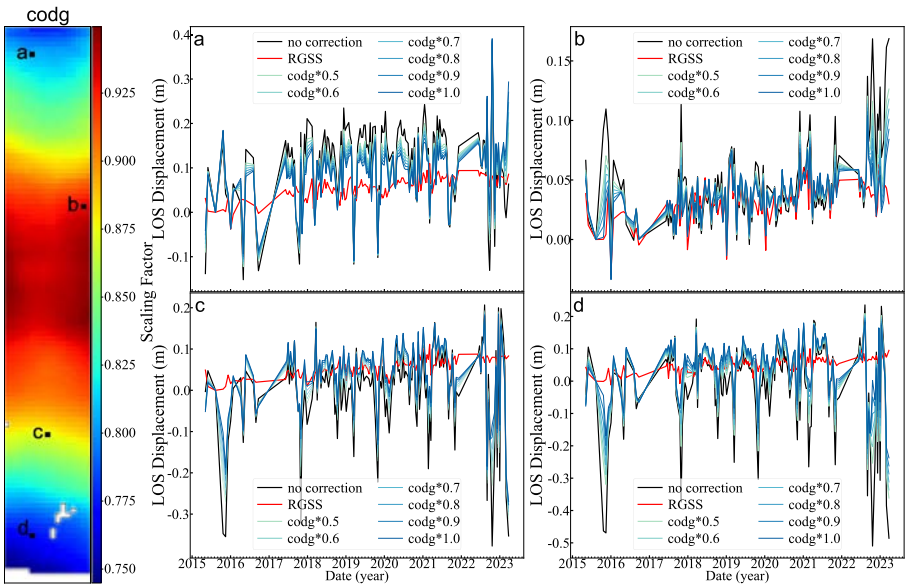

Fig. 20 Left panel: Temporally averaged scaling factor by comparing the ionospheric phases estimated by the range split-spectrum method and GIMs (see the supplementary information for details). Right panels: **a**–**d** are LOS deformation times series at the four locations labeled in the left panel with and without corrections using the range split-spectrum method and GIMs with different scaling factors. The GIMs used are codg. The data are from track A149 in northern Chile

Table 5 RMS between CGPS velocities and InSAR velocities corrected using the range split-spectrum method and GIMs with different scaling factors. The unit is mm/yr. The data are from track A41 on the Tibetan Plateau

No correction	Range split-spectrum method	GIM	Scaling factor					
			0.5	0.6	0.7	0.8	0.9	1.0
9.16	1.89	jplg	3.40	2.94	3.09	3.78	4.78	5.94
		codg	3.14	2.49	2.49	3.14	4.16	5.33
		esag	4.31	3.50	2.84	2.47	2.53	2.98
		igsg	4.15	3.28	2.58	2.20	2.31	2.85
		emrg	5.08	4.33	3.65	3.07	2.65	2.49
		upcg	5.24	4.49	3.78	3.12	2.55	2.15
		uqrg	6.22	5.65	5.09	4.54	4.01	3.51
		casg	3.86	3.14	2.78	2.92	3.50	4.35
		jpld	4.17	3.88	4.04	4.61	5.46	6.48

1 9
RMS (mm/yr)

reveal that no single globally optimal scaling factor exists. Instead, we observe a fundamental trade-off: Smaller factors (e.g., 0.7) better suppress errors inherent in the GIMs but tend to under-correct strong ionospheric signals; larger factors (e.g., 0.9) more effectively remove the ionospheric phase but are more susceptible to amplifying GIM errors. Consequently, for long time series spanning diverse ionospheric conditions, a fixed scaling factor is not always effective and may, in some cases, introduce additional errors. This limitation motivates the development of an empirical adaptive scaling factor.

As shown in Fig. 20, the scaling factor exhibits substantial spatiotemporal variability. This variability is not merely a mathematical artifact but reflects the physical complexity of the ionosphere. The thin-shell approximation adopted in GIMs (typically fixed at 450 km) simplifies a vertically stratified medium that extends from approximately 50 to 1000 km altitude, with electron density varying continuously with height. The electron density profile varies with location, time of day, season, and solar activity, and typically peaks around an altitude of 400 km.

In principle, the scaling factor should vary both spatially and temporally. However, given the limited experimental regions, we cannot fully characterize its spatial variability. We therefore focus on developing an empirical adaptive scaling factor that varies with time. In previous works, Zhang et al. (2022) introduced an empirical adaptive scaling factor modeled as a sixth-order polynomial that captures seasonal variations. More recently, Gisinger et al. (2025) found that over longer timescales, the 11-year solar cycle exerts a stronger influence on the scaling factor than seasonal variations. Here, we test four empirical adaptive scaling factor models for three ascending tracks: A 6th-order polynomial and an 11-year periodic sinusoidal function, both as a function of the number of days relative to the solar minimum on December 15, 2019 (focusing on long-term effects); A 6th-order polynomial and a 1-year periodic sinusoidal function, both as a function of the day of year (focusing on seasonal effects).

Table 6 RMS between CGPS velocities and InSAR velocities corrected using the GIMs with two fixed scaling factors and an empirical adaptive scaling factor. The scaling factor 'A' denotes the empirical adaptive scaling factor. 'RGSS' denotes the range split-spectrum method

Track	A149			A149_half_cycle			A41			A12		
Scaling factor	0.69	0.9	A	0.69	0.9	A	0.69	0.9	A	0.69	0.9	A
No correction	3.43			6.95			9.16			6.81		
Corrected by RGSS	2.07			2.52			1.89			2.03		
Corrected by codg	3.30	3.38	3.15	5.94	6.02	5.25	2.45	4.16	2.51	2.35	2.59	2.27
Corrected by jplg	3.82	4.06	3.81	6.20	6.36	5.37	3.05	4.78	3.24	2.32	3.91	2.74
Corrected by jpld	2.83	2.87	2.59	5.07	4.83	4.22	4.00	5.46	4.41	2.24	4.09	2.76
Corredted by uqrg	3.09	3.24	2.80	5.12	5.31	2.85	5.14	4.01	5.59	4.94	4.40	5.31

1 9
RMS (mm/yr)

To estimate the empirical adaptive scaling factor, we use the ionospheric phases estimated from the range split-spectrum method and derived from codg. A direct comparison is not possible, however, because the range split-spectrum method can only estimate a relative ionospheric phase, both spatially and temporally. To address the spatially relative nature, we remove a spatial reference value from each ionospheric phase image. For both the range split-spectrum and codg-derived phases, we subtract the phase value of a common reference pixel locating at the image center from all pixels. To address the temporally relative nature, we reconstruct absolute time series from the relative range split-spectrum estimates. We first subtract the ionospheric phase of the first acquisition date from all range split-spectrum estimates and then add the codg-derived ionospheric phase for the first date (computed with a scaling factor of 0.9). After these corrections, the range split-spectrum and GIM-derived ionospheric phases are directly comparable.

The ratio between the adjusted ionospheric phases from the range split-spectrum method and codg is then used to estimate the scaling factor. To account for spatial variability and mitigate the influence of outliers, we retain only the central 80% of the ratio values for each date and take their median as the representative scaling factor. As shown in Fig. S16, the scaling factor exhibits a clear temporal structure rather than random scatter, validating the approach of modeling it as a function of acquisition date. The scaling factor sometimes exceeds 1. This is possible as the GIM is a smoothed low-resolution representation of the true TEC.

Next, we fit the data with the four candidate models. The model parameters are estimated using data from ascending tracks A41 and A12 on the Tibetan Plateau, and the results are presented in Fig. S16 in the supplementary information. The performance of the derived models is evaluated for three ascending tracks including A41, A12 and A149, with the results summarized in Table S12. The long-term models, which account for solar cycle effects, consistently outperform the seasonal models. The polynomial and sinusoidal long-term models yield similar performance. Considering model stability, we select the 11-year sinusoidal model shown in Fig. 21 for estimating the empirical adaptive scaling factor. The model is expressed as

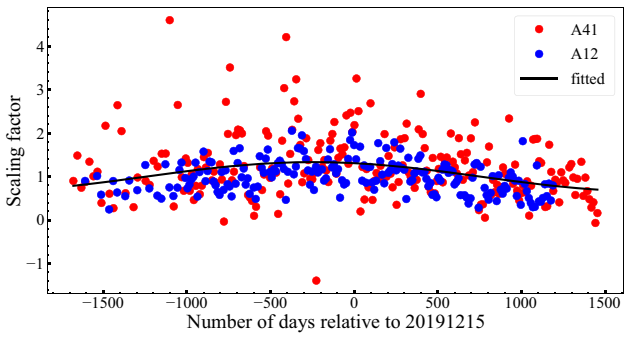

Fig. 21 Empirical adaptive scaling factor derived using the ionospheric phases estimated by the range split-spectrum method and codg GIMs. The results are for Tracks A41 and A12 on the Tibetan Plateau

$$\alpha_{\text{adaptive}} = -0.33554523 \times \sin(0.001564 \times \text{date} - 1.18897913) + 0.99633983 \quad (2)$$

where date is the number of days relative to 20191215. Its performance in correcting InSAR time series is summarized in Table 6.

The empirical adaptive scaling factor improves velocity estimates in the majority of cases. In particular, the model parameters estimated from Tibetan Plateau tracks can also improve the results in northern Chile, demonstrating a degree of applicability across geographical regions. A more comprehensive characterization of the scaling factor's global variability could potentially yield further improvements, but this is beyond the scope of the present study.

5 Role of the time span of InSAR time series relative to solar cycle

The TEC in the ionosphere is primarily a result of solar radiation directly related to solar activity with a cycle of about 11 years. Solar activity is commonly quantified using sunspot

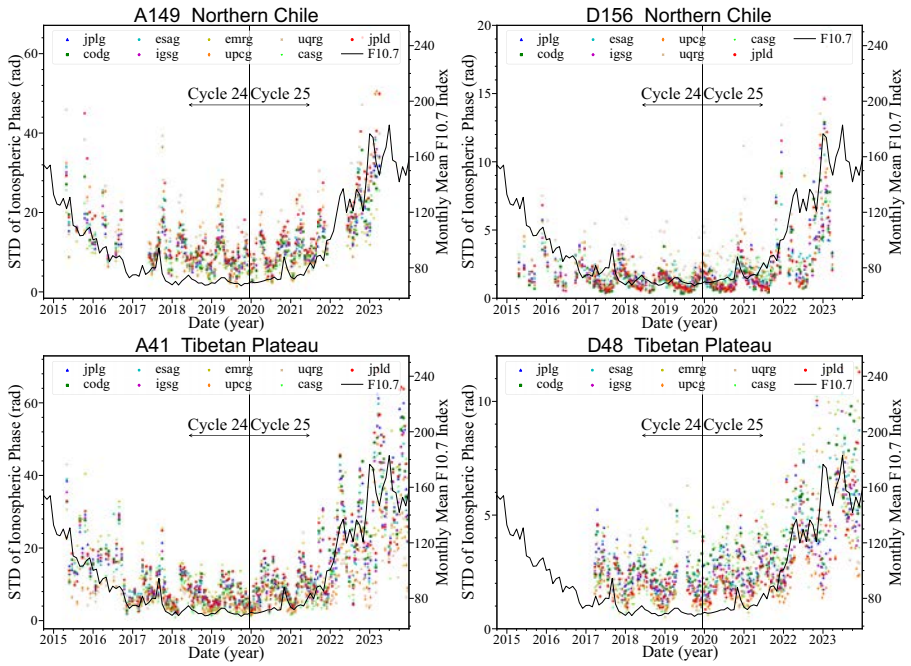

Fig. 22 Comparison between the F10.7 index and the spatial standard deviation of the ionospheric phases from GIMs

numbers and the 10.7 cm Solar Radio Flux (F10.7 index). The F10.7 index, which measures solar radio emission intensity at a wavelength of 10.7 cm (2800 MHz), serves as an excellent proxy for solar Extreme Ultraviolet (EUV) radiation. Higher F10.7 values indicate stronger solar activity and enhanced EUV flux, leading to increased ionization and thus higher TEC. The F10.7 index has proven valuable in specifying and forecasting space weather and correlates strongly with sunspot number. In Figs. 22 and S17, we compare the F10.7 index and spatial standard deviations of the ionospheric phases derived from different GIMs over our study period (2014–2023). The correlation between the F10.7 index and the ionospheric phase is evident.

Because the solar activity varies cyclically with a period of 11 years, ionospheric effects exhibit corresponding cyclic behavior. Consequently, the impact of the ionospheric phase on the mean velocity of deformation time series depends on the time span of the time series relative to the solar cycle. We therefore examine the ionospheric correction results of InSAR time series spanning different periods of the solar cycle to investigate this dependence. According to the record of the number of sunspots, the maximum of solar cycle 24 occurred in April 2014, with a maximum of the 13-month smoothed sunspot number at 81.8[3], and the following solar minimum occurred in December 2019, with the 13-month smoothed sunspot number fell to 1.8[4]. The maximum of solar cycle 25 occurred in October 2024 with the 13-month smoothed sunspot number at 160.8[5], nearly twice the maximum in solar cycle 24. Based on these solar maximum and minimum times, we examine time series with different time spans. Each time span includes two segments: a pre-minimum period (from a selected start date to December 2019) and a post-minimum period (from December 2019 to a selected end date). We experiment with different ratios of pre- to post-minimum durations, including 1:1, 1:2 and 2:1. For each ratio, we also test different numbers of acquisitions in the time span. Table 7 lists the RMS errors of the mean deformation velocities compared with CGPS measurements for track A149 in northern Chile. Results for other tracks can be found in Tables S13–S17.

These experiments demonstrate that the impact of ionospheric phase on mean velocity estimates depends strongly on the time span relative to the solar cycle. Generally, when the time span is approximately symmetric about solar minimum (pre- to post-minimum ratio of 1:1), the ionospheric effects are largely averaged out in the mean velocity estimates. The ionospheric effects of period ratio 1:2 are much stronger than those of period ratio 2:1. This asymmetry arises because Solar Cycle 25 is significantly more active than Cycle 24, as evidenced by the higher sunspot numbers[6] and the F10.7 index during the post-minimum period. As the magnitude of the ionospheric phases increases, the GIM correction becomes more effective. Consistent with earlier findings, jpld exhibits the best performance among the GIMs.

[3] https://www.sidc.be/SILSO/news004

[4] https://www.weather.gov/news/201509-solar-cycle

[5] https://www.sidc.be/article/sc25-maximum-october-2024

[6] https://www.swpc.noaa.gov/products/solar-cycle-progression

Table 7 RMS of the mean deformation velocities of time series with different time spans relative to the solar cycle. The data are from track A149 in northern Chile

Period ratio	Start date	End date	Number of dates	No correction	Corrected by range split-spectrum method	Corrected by codg with a scaling factor 0.9	Corrected by GIMs with an empirical adaptive scaling factor			
							codg	jplg	jpld	uqrg
1:1	20160829	20230326	144	6.82	2.16	6.24	5.44	6.90	3.83	4.06
	20170607	20220623	122	2.51	2.09	2.46	2.53	2.45	2.49	2.24
	20180214	20211008	101	3.47	2.46	2.98	3.43	3.29	2.59	3.85
	20180720	20210517	77	4.64	3.35	3.43	3.77	3.93	3.13	4.53
	20190209	20201013	46	9.17	4.36	7.97	8.62	9.69	5.55	20.42
1:2	20180427	20230326	120	9.71	2.31	8.46	7.46	8.99	4.33	5.08
	20180720	20221009	103	5.75	2.03	4.68	4.46	4.04	2.90	2.56
	20180918	20220611	89	6.39	2.47	3.20	3.73	4.44	2.82	5.50
	20190221	20210809	69	3.96	3.49	3.62	4.14	4.41	3.27	12.84
	20190516	20210210	47	9.30	5.22	6.72	6.30	6.21	5.18	5.16
2:1	20160102	20211207	128	2.08	2.04	2.02	2.02	2.17	2.30	2.07
	20160829	20210809	114	2.86	2.26	2.49	2.44	2.59	2.98	2.89
	20170701	20210306	97	4.20	2.49	3.23	2.96	3.53	3.02	2.61
	20180214	20201118	75	3.33	3.07	3.02	3.26	3.09	2.97	3.50
	20180930	20200721	49	12.38	4.84	8.01	6.78	11.55	6.31	16.25
other	20150507	20191218	81	6.88	2.46	6.07	5.52	5.58	4.35	2.99
	20191218	20230326	76	19.60	2.83	17.12	15.32	19.18	8.52	12.29
	20150507	20230326	156	3.43	2.07	3.38	3.15	3.81	2.59	2.80

40 200 Number of Dates

1 9 RMS (mm/yr)

6 Conclusions

We have comprehensively evaluated the performance of eight available IGS GIMs, a high-resolution GIM from JPL and ESA's ETAD for correcting ionospheric effects in Earth's surface motion measurements from C-band InSAR. From the evaluation, we find:

(1) GIMs can generally perform effective ionospheric correction for individual interferograms and improve the mean velocity estimate, with the magnitude of the improvement scaling with the strength of the ionospheric phase. When the ionospheric phase is small, such as for data acquired in the midlatitude regions on descending tracks of the dawn-dusk orbit used by Sentinel-1, applying GIM corrections may instead degrade the result. In such cases, we do not recommend using GIMs for ionospheric correction, because the ionospheric effect is generally negligible. Their performance also exhibits geographical variability. For example, in some coastal regions, where the density of IGS stations is sparse, the IGS GIMs show reduced effectiveness. The correction performance further depends on the temporal alignment between the SAR acquisition time and the GIM product times, underscoring the need for improving the temporal resolution of IGS GIM products.

(2) jpld generally performs much better than the IGS GIMs. Occasionally, it even outperforms the range split-spectrum method. It improves velocity estimates in nearly all instances; the sole exception occurs where the ionospheric signal is negligible, and applying any correction slightly degrades the result. Its superior performance is likely attributed to its much higher temporal and spatial resolutions, compared to the IGS GIMs. This evaluation highlights the value of improving GIM resolutions, as carried out by JPL.

(3) Among the IGS GIMs, codg, which is used in ESA's ETAD products, exhibits the most stable and best overall performance for InSAR ionospheric correction, followed by jplg. uqrg, which has a relatively high temporal resolution and performs well in GNSS-based validation studies, shows better performance in regions with rapid ionospheric variations, but its performance is less stable.

(4) The scaling factor exhibits significant spatiotemporal variability, precluding the existence of a single globally optimal value. An empirical adaptive scaling factor that varies with acquisition date outperforms fixed factors in time series analysis, with the improvement being most pronounced for long time spans.

(5) The impact of the ionospheric phase on mean velocity estimates depends strongly on the time span of the time series relative to the 11-year solar cycle. The ionospheric signal largely averages out in the mean velocity estimate, when the time span is symmetric about the solar minimum or maximum.

Our evaluations not only validate current GIMs from the unique perspective of high-resolution spaceborne radar, but also provide useful feedback to the GIM development community. The primary limitations of the corrections originate from the errors and the low spatial and temporal resolutions of GIMs. Therefore, our findings underscore the need for continued efforts to improve GIM resolution, as exemplified by the development of the high-resolution jpld products at JPL (Martire et al. 2024). A particularly promising avenue for future work would be to incorporate tens of thousands of globally distributed continuous GNSS stations (Blewitt et al. 2018) into the current IGS network, potentially enabling the generation of GIMs with substantially improved spatial and temporal resolutions and, consequently, more accurate ionospheric corrections for InSAR.

Supplementary Information The online version contains supplementary material available at https://doi.org/10.1007/s00190-026-02084-3.

Acknowledgements InSAR processing is performed using ISCE2 (https://github.com/isce-framework/isce2), and time series analysis is performed using MintPy (https://github.com/insarlab/MintPy). Figures are mostly generated using GMT (Wessel et al. 2019). We thank Christoph Gisinger of the Remote Sensing Technology Institute, German Aerospace Center, for discussions on ESA's ETAD products.

Author contributions Conceptualization: Cunren Liang; Methodology: Xue Li, Cunren Liang; Formal analysis and investigation: Xue Li, Cunren Liang; Funding acquisition: Cunren Liang; Resources: Xue Li, Jiafeng Li, Kejie Chen; Supervision: Cunren Liang; Writing—original draft preparation: Xue Li, Cunren Liang; Writing—review and editing: all authors.

Funding National Natural Science Foundation of China under Grants 42274026 and 42474046 and Ministry of Natural Resources South China Landslide Risk Field Scientific Observation and Research Station Driven by Climate Change funded this work.

Data availability Sentinel-1 data are available at the Alaska Data Search Vertex (https://search.asf.alaska.edu). IGS GIMs are available at the IGS ionosphere products website (https://cddis.nasa.gov/archive/gnss/products/ionex/). jpld GIMs are available at the JPL ionospheric products website (https://sideshow.jpl.nasa.gov/pub/iono_daily/gim_for_research/jpld/). NGL CGPS data are available at the NGL website (http://geodesy.unr.edu/gps_timeseries/tenv3/IGS14/). Sunspot number data are available at the SIDC website (https://www.sidc.be/SILSO/datafiles). The 10.7 cm solar radio flux data are available at the GFZ Helmholtz Centre for Geosciences website (https://kp.gfz.de/en/data).

Declarations

Conflict of interest The authors have no competing interests to declare that are relevant to the content of this article.

References

Angermann D, Klotz J, Reigber C (1999) Space-geodetic estimation of the Nazca-South America euler vector. Earth Planet Sci Lett 171:329–334. https://doi.org/10.1016/s0012-821x(99)00173-9

Ansari H, De Zan F, Parizzi A (2021) Study of systematic bias in measuring surface deformation with SAR interferometry. IEEE Trans Geosci Remote Sens 59:1285–1301. https://doi.org/10.1109/TGRS.2020.3003421

Balss U, Gisinger C, Eineder M (2018) Measurements on the absolute 2-D and 3-D localization accuracy of TerraSAR-X. Remote Sens 10(656):1–21

Blewitt G, Hammond WC, Kreemer C (2018) Harnessing the GPS data explosion for interdisciplinary science. Eos. https://doi.org/10.1029/2018EO104623

Blewitt G (2024) An improved equation of latitude and a global system of graticule distance coordinates. J Geod 98:6–6. https://doi.org/10.1007/s00190-023-01815-0

Brcic R, Parizzi A, Eineder M, Bamler R, Meyer F (2010) Estimation and compensation of ionospheric delay for SAR interferometry. In Proc. 2010 IEEE Int Geosci Remote Sens Symp 2908–2911. https://doi.org/10.1109/IGARSS.2010.5652231

Cao Y, JónssonSigurjón Li Z (2021) Advanced InSAR tropospheric corrections from global atmospheric models that incorporate spatial stochastic properties of the troposphere. J Geophys Res Solid Earth. https://doi.org/10.1029/2020JB020952

Chen P, Zhang Y, Wang R, An Z, Yao Y (2023) A novel approach for establishing the global ionospheric model with high spatiotemporal resolution. IEEE Trans Geosci Remote Sens. https://doi.org/10.1109/TGRS.2023.3238044

Chlieh M, de Chabalier JB, Ruegg JC, Armijo R, Dmowska R, Campos J, Feigl KL (2004) Crustal deformation fault slip during the seismic cycle in the North Chile subduction zone, from GPS and InSAR observations. Geophys J Int 158:695–711. https://doi.org/10.1111/j.1365-246X.2004.02326.x

Contreras-Reyes E, Jara J, Grevemeyer I, Ruiz S, Carrizo D (2012) Abrupt change in the dip of the subducting plate beneath North Chile. Nat Geosci 5:342–345. https://doi.org/10.1038/NGEO1447

Delouis B, Nocquet J, Vallee M (2010) Slip distribution of the February 27, 2010 mw = 8.8 Maule earthquake, central Chile, from static and high-rate GPS, InSAR, and broadband teleseismic data. Geophys Res Lett. https://doi.org/10.1029/2010GL043899

DeMets C, Gordon RG, Argus DF, Stein S (1990) Current plate motions. Geophys J Int 101:425–478. https://doi.org/10.1111/j.1365-246X.1990.tb06579.x

Dewey JF, Burke KC (1973) Tibetan, variscan, and precambrian basement reactivation: products of continental collision. J Geol 81:683–692. https://doi.org/10.1086/627920

Elliott JR, Walters RJ, England PC, Jackson JA, Li Z, Parsons B (2010) Extension on the Tibetan Plateau: Recent normal faulting measured by InSAR and body wave seismology: extension on the Tibetan Plateau. Geophys J Int 183:503–535. https://doi.org/10.1111/j.1365-246X.2010.04754.x

Erdogan E, Schmidt M, Seitz F, Durmaz M (2017) Near real-time estimation of ionosphere vertical total electron content from GNSS satellites using B-splines in a kalman filter. Ann Geophys 35:263–277. https://doi.org/10.5194/angeo-35-263-2017

Fattahi H, Amelung F (2013) DEM error correction in InSAR time series. IEEE Trans Geosci Remote Sens 51:4249–4259. https://doi.org/10.1109/TGRS.2012.2227761

Fattahi H, Simons M, Agram P (2017) InSAR time-series estimation of the ionospheric phase delay: an extension of the split range-spectrum technique. IEEE Trans Geosci Remote Sens 55:5984–5996

Farr TG, Rosen PA, Caro E, Crippen R, Duren R, Hensley S, Kobrick M, Paller M, Rodriguez E, Roth L, Seal D, Shaffer S, Shimada J, Umland J, Werner M, Oskin M, Burbank D, Alsdorf D (2007) The shuttle radar topography mission. Rev Geophys. https://doi.org/10.1029/2005RG000183

Feltens J (2007) Development of a new three-dimensional mathematical ionosphere model at European Space Agency/European Space

Operations Centre. Sp Weather. https://doi.org/10.1029/2006SW000294
Gisinger C, Libert L, Marinkovic P, Krieger L, Larsen Y, Valentino A, Breit H, Balss U, Suchandt S, Nagler T, Eineder M, Miranda N (2022) The extended timing annotation dataset for sentinel-1-product description and first evaluation results. IEEE Trans Geosci Remote Sens 60:1–22. https://doi.org/10.1109/TGRS.2022.3194216
Gisinger C, Balss U, Breit H (2023). S1-ETAD Algorithm technical baseline document. ETAD-DLR-DD-0008, 23: 1–54.
Gisinger C, Gomba G, Hoque M, Navarro V, Valentino A, Pinheiro M, Hajduch G, Bleriot R (2025). Impact Of 25-th Solar Cycle Ionospheric Activity On Sentinel-1 SAR Data – A Status Report By SAR-MPC. ESA Living Planet Symposium 2025, Vienna, Austria.
Ghoddousi-Fard R, Héroux P, Danskin D, Boteler D (2011) Developing a GPS TEC mapping service over Canada. Sp Weather. https://doi.org/10.1029/2010SW000621
Goldstein RM, Engelhardt H, Kamb B, Frolich RM (1993) Satellite radar interferometry for monitoring ice sheet motion; application to an antarctic ice stream. Sci (American Association for the Advancement of Science) 262:1525–1530. https://doi.org/10.1126/science.262.5139.1525
Gomba G, Parizzi A, De Zan F, Eineder M, Bamler R (2016) Toward operational compensation of ionospheric effects in SAR interferograms: the split-spectrum method. IEEE Trans Geosci Remote Sens 54:1446–1461. https://doi.org/10.1109/TGRS.2015.2481079
Goss A, Schmidt M, Erdogan E, Seitz F (2020) Global and regional high-resolution VTEC modelling using a two-step B-spline approach. Remote Sens 12:1198. https://doi.org/10.3390/rs12071198
Grandin R, Doin M, Bollinger L, Pinel-Puyssegur B, Ducret G, Jolivet R, Sapkota SN (2012) Long-term growth of the himalaya inferred from interseismic InSAR measurement. Geol (Boulder) 40:1059–1062. https://doi.org/10.1130/G33154.1
Gray AL, Mattar KE, Sofko G (2000) Influence of ionospheric electron density fluctuations on satellite radar interferometry. Geophys Res Lett 27:1451–1454. https://doi.org/10.1029/2000GL000016
Hernández-Pajares M, Juan JM, Sanz J (1999) New approaches in global ionospheric determination using ground GPS data. J Atmos Sol-Terr Phys 6826(99):1237–1247. https://doi.org/10.1016/S1364-6826(99)00054-1
Hernández-Pajares M, Juan JM, Sanz J, Orus R, Garcia-Rigo A, Feltens J, Komjathy A, Schaer SC, Krankowski A (2009) The IGS VTEC maps: a reliable source of ionospheric information since 1998. J Geod 83:263–275. https://doi.org/10.1007/s00190-008-0266-1
Hernández-Pajares M, Roma-Dollase D, Krankowski A, García-Rigo A, Orús-Pérez R (2017) Methodology and consistency of slant and vertical assessments for ionospheric electron content models. Jgeod 91:1405–1414. https://doi.org/10.1007/s00190-017-1032-z
Hu Z, Fan L, Wang C, Wang Z, Shi C, Jing G (2020) More reliable global ionospheric maps combined from ionospheric products of the seven IGS analysis centers. Results Phys 17:103162. https://doi.org/10.1016/j.rinp.2020.103162
Jolivet R, Agram PS, Lin NY, Simons M, Doin M-P, Peltzer G, Li Z (2014) Improving InSAR geodesy using Global Atmospheric Models. J Geophys Res Solid Earth 119:2324–2341. https://doi.org/10.1002/2013JB010588
Kelleher JA (1972) Rupture zones of large south american earthquakes and some predictions. J Geophys Res 77:2087–2103. https://doi.org/10.1029/JB077i011p02087
Lemrabet L, Doin MP, Lasserre C, Durand P (2023) Referencing of continental-scale InSAR-derived velocity fields: case study of the eastern Tibetan Plateau. J Geophys Res: Solid Earth 128(7):e2022JB026251
Li Z, Yuan Y, Wang N, Hernandez-Pajares M, Huo X (2015) SHPTS: Towards a new method for generating precise global ionospheric TEC map based on spherical harmonic and generalized trigonometric series functions. J Geod 89:331–345. https://doi.org/10.1007/s00190-014-0778-9
Liang C, Fielding EJ (2017) Measuring azimuth deformation with L-band ALOS-2 ScanSAR interferometry. IEEE Trans Geosci Remote Sens 55:2725–2738. https://doi.org/10.1109/TGRS.2017.2653186
Liang C, Agram P, Simons M, Fielding EJ (2019) Ionospheric correction of InSAR time series analysis of C-band sentinel-1 TOPS data. IEEE Trans Geosci Remote Sens 57:6755–6773. https://doi.org/10.1109/TGRS.2019.2908494
Lomnitz C (1970) Major earthquakes and tsunamis in Chile during the period 1535 to 1955. Geol Rundsch 59:938–960. https://doi.org/10.1007/bf02042278
Luzum B, Petit G (2012) The IERS conventions (2010): Reference systems and new models. Proc Int Astron Union 10:227–228. https://doi.org/10.1017/S1743921314005535
Mannucci AJ, Wilson BD, Yuan DN, Ho CH, Lindqwister UJ, Runge TF (1998) A global mapping technique for GPS-derived ionospheric total electron content measurements. Radio Sci 33:565–582. https://doi.org/10.1029/97RS02707
Mannucci AJ, Iijima B, Sparks L, Pi X, Wilson B, Lindqwister U (1999) Assessment of global TEC mapping using a three-dimensional electron density model. J Atmos Sol-Terr Phys 61(16):1227–1236. https://doi.org/10.1016/s1364-6826(99)00053-x
Marconato L, Doin MP, Lovery B, Rolland L, Durand P (2025) Long-wavelength ionospheric compensation of InSAR time-series based on Global ionosphere maps. Geophys Res Lett 52(23):e2025GL118843
Martire L, Runge TF, Meng X, Krishnamoorthy S, Vergados P, Mannucci AJ, Verkhoglyadova OP, Komjáthy A, Moore AW, Meyer RF, Ijima BA, Green DW (2024) The JPL-GIM algorithm and products: multi-GNSS high-rate global mapping of total electron content. J Geod 98:44. https://doi.org/10.1007/s00190-024-01860-3
Massonnet D, Rossi M, Carmona C, Adragna F, Peltzer G, Feigl K, Rabaute T (1993) The displacement field of the landers earthquake mapped by radar interferometry. Nat (London) 364:138–142. https://doi.org/10.1038/364138a0
Milbert D (2018) Solid: Solid Earth Tide. [Software]. Available: http://geodesyworld.github.io/SOFTS/solid.htm
Molnar P, Tapponnier P (1978) Active tectonics of Tibet. J Geophys Res 83:5361–5375. https://doi.org/10.1029/JB083iB11p05361
Molnar P, Chen W-P (1983) Focal depths and fault plane solutions of earthquakes under the Tibetan Plateau. J Geophys Res Solid Earth 88:1180–1196. https://doi.org/10.1029/JB088iB02p01180
Orús R, Hernández-Pajares M, Juan JM, Sanz J (2005) Improvement of global ionospheric VTEC maps by using Kriging interpolation technique. J Atmos Sol-Terr Phys 67:1598–1609. https://doi.org/10.1016/j.jastp.2005.07.017
Ou Q, Daout S, Weiss JR, Shen L, Lazecký M, Wright TJ, Parsons BE (2022) Large-scale interseismicstrain mapping of the NE Tibetan Plateau from Sentinel-1 interferometry. J Geophys Res Solid Earth 127:e2022JB024176. https://doi.org/10.1029/2022JB024176
Peltzer G, Rosen P (1995) Surface displacement of the 17 May 1993 eureka valley, california, earthquake observed by SAR interferometry. Sci (American Association for the Advancement of Science) 268:1333–1336. https://doi.org/10.1126/science.268.5215.1333
Peltzer G, Crampé F, King G (1999) Evidence of Nonlinear Elasticity of the Crust from the Mw7.6 Manyi (Tibet) Earthquake. Sci 286:272–276. https://doi.org/10.1126/science.286.5438.272
Peter H, Pastor R, Aguilar J, Femandez J (2021) Copernicus POD product handbook. GMV-CPOD-TN-0009.

Pritchard ME, Simons M, Rosen PA, Hensley S, Webb FH (2002) Co-seismic slip from the 1995 July 30 mw= 8.1 antofagasta, Chile, earthquake as constrained by InSAR and GPS observations. Geophys J Int 150:362–376. https://doi.org/10.1046/j.1365-246X.2002.01661.x

Pritchard ME, Simons M (2004) An InSAR-based survey of volcanic deformation in the central andes. Geochem Geophys Geosyst 5:Q02002. https://doi.org/10.1029/2003GC000610

Rosen PA, Hensley S, Chen C (2010) Measurement and mitigation of the ionosphere in L-band interferometric SAR data. In Proc IEEE Radar Conf. https://doi.org/10.1109/RADAR.2010.5494385

Schaer S (1999) Mapping and predicting the Earth's ionosphere using the global positioning system. Ph.D. dissertation, Astron. Inst., Univ. Bern, Bern, Switzerland.

Stephenson OL, Liu Y, Zhang Y, Simons M, Rosen P, Xu X (2022) The impact of plate motions on long-wavelength InSAR-derived velocity fields. Geophys Res Lett. https://doi.org/10.1029/2022GL099835

Tong X, Sandwell DT, Smith-Konter B (2013) High-resolution interseismic velocity data along the san andreas fault from GPS and InSAR. J Geophys Res Solid Earth 118:369–389. https://doi.org/10.1029/2012JB009442

Wang M, Shen ZK (2020) Present-day crustal deformation of continental China derived from GPS and its tectonic implications. J Geophys Res Solid Earth 125:e2019018774. https://doi.org/10.1029/2019JB018774

Watson AR, Elliott JR, Walters RJ (2022) Interseismic strain accumulation across the main recent fault, SW iran, from sentinel-1 InSAR observations. J Geophys Res Solid Earth. https://doi.org/10.1029/2021JB022674

Watson AR, Elliott JR, Lazecky M, Maghsoudi Y, McGrath JD, Walters RJ (2024) An InSAR-GNSS velocity field for Iran. Geophys Res Lett. https://doi.org/10.1029/2024GL108440

Weiss JR, Walters RJ, Morishita Y, Wright TJ, Lazecky M, Hua W, Hussain E, Hooper AJ, Elliott JR, Rollins C, Chen Y, Gonzalez PJ, Spaans K, Li Z, Parsons B (2020) High-resolution surface velocities and strain for anatolia from sentinel-1 InSAR and GNSS data. Geophys Res Lett. https://doi.org/10.1029/2020GL087376

Wessel P, Luis JF, Uieda L, Scharroo R, Wobbe F, Smith WHF, Tian D (2019) The generic mapping tools version 6. Geochem Geophys Geosyst 20:5556–5564. https://doi.org/10.1029/2019GC008515

Wright TJ, Parsons B, England PC, Fielding EJ (2004) InSAR observations of low slip rates on the major faults of western Tibet. Sci 305:236–239

Xu X, Sandwell DT, Klein E, Bock Y (2021) Integrated Sentinel-1 InSAR and GNSS time-series alongthe San Andreas fault system. J Geophys Res Solid Earth 126:e2021022579. https://doi.org/10.1029/2021JB022579

Yague-Martinez N, Prats-Iraola P, Rodriguez Gonzalez F, Brcic R, Shau R, Geudtner D, Eineder M, Bamler R (2016) Interferometric processing of sentinel-1 TOPS data. IEEE Trans Geosci Remote Sens 54:2220–2234. https://doi.org/10.1109/TGRS.2015.2497902

Yu C, Li Z, Penna NT, Crippa P (2018) Generic atmospheric correction model for interferometric synthetic aperture radar observations. J Geophys Res Solid Earth 123:9202–9222. https://doi.org/10.1029/2017JB015305

Zebker HA, Rosen PA, Hensley S (1997) Atmospheric effects in interferometric synthetic aperture radar surface deformation and topographic maps. J Geophys Res 102:7547–7563. https://doi.org/10.1029/96JB03804

Zhang H, Xu P, Han W, Ge M, Shi C (2013) Eliminating negative VTEC in global ionosphere maps using inequality-constrained least squares. Adv Space Res 51:988–1000. https://doi.org/10.1016/j.asr.2012.06.026

Zhang Y, Fattahi H, Amelung F (2019) Small baseline InSAR time series analysis; unwrapping error correction and noise reduction. Comput Geosci 133:104331. https://doi.org/10.1016/j.cageo.2019.104331

Zhang Y, Fattahi H, Pi X, Rosen P, Simons M, Agram P, Aoki Y (2022) Range geolocation accuracy of C-/L-band SAR and its implications for operational stack coregistration. IEEE Trans Geosci Remote Sens 60:1–19. https://doi.org/10.1109/TGRS.2022.3168509

Zheng Y, Fattahi H, Agram P, Simons M, Rosen P (2022) On closure phase and systematic bias in multilooked SAR interferometry. IEEE Trans Geosci Remote Sens 60:1–11. https://doi.org/10.1109/TGRS.2022.3167648

Publisher's Note Springer Nature remains neutral with regard to jurisdictional claims in published maps and institutional affiliations.

Springer Nature or its licensor (e.g. a society or other partner) holds exclusive rights to this article under a publishing agreement with the author(s) or other rightsholder(s); author self-archiving of the accepted manuscript version of this article is solely governed by the terms of such publishing agreement and applicable law.

Supplementary Information for

An evaluation of Global Ionosphere Maps for the ionospheric correction of C-band InSAR data

Xue Li[1], Cunren Liang[1,*], Jiafeng Li[2], and Kejie Chen[3]

[1]Institute of Remote Sensing and Geographic Information System, School of Earth and Space Sciences, Peking University, Beijing 100871 China.

[2]School of Geodesy and Geomatics, Wuhan University, Wuhan 430072 China.

[3]Department of Earth and Space Sciences, Southern University of Science and Technology, Shenzhen 518055 China.

[*]Corresponding author, e-mail: cunren.liang@pku.edu.cn

1 Tables

Table S1 Proportions of high-, moderate-, and low-quality ionospheric estimates derived from GIMs for individual interferograms of track A149 in northern Chile (scaling factor = 0.9)

GIM	High-quality	Moderate-quality	Low-quality
jplg	6.50%	62.00%	31.50%
codg	11.00%	57.50%	31.50%
esag	5.00%	59.00%	36.00%
igsg	5.50%	58.50%	36.00%
emrg	2.00%	49.00%	49.00%
upcg	2.00%	37.00%	61.00%
uqrg	12.00%	44.50%	43.50%
casg	6.50%	56.50%	37.00%
jpld	19.00%	53.50%	27.50%

0% 100%

Table S2 Proportions of high-, moderate-, and low-quality ionospheric estimates derived from GIMs for individual interferograms of track D156 in northern Chile (scaling factor = 0.9)

GIM	High-quality	Moderate-quality	Low-quality
jplg	7.00%	67.50%	25.50%
codg	7.00%	69.00%	24.00%
esag	4.50%	65.50%	30.00%
igsg	4.00%	64.00%	32.00%
emrg			
upcg	1.00%	67.50%	31.50%
uqrg	2.00%	36.50%	61.50%
casg	3.00%	64.50%	32.50%
jpld	10.50%	69.50%	20.00%

0% 100%

Table S3 Proportions of high-, moderate-, and low-quality ionospheric estimates derived from GIMs for individual interferograms of track A41 on the Tibetan Plateau (scaling factor = 0.9)

GIM	High-quality	Moderate-quality	Low-quality
jplg	5.50%	69.50%	25.00%
codg	3.50%	71.00%	25.50%
esag	4.50%	63.50%	32.00%
igsg	4.00%	60.00%	36.00%
emrg	1.50%	64.00%	34.50%
upcg	7.00%	61.00%	32.00%
uqrg	2.50%	35.50%	62.00%
casg	3.00%	59.50%	37.50%
jpld	5.50%	62.00%	32.50%

0% 100%

Table S4 Proportions of high-, moderate-, and low-quality ionospheric estimates derived from GIMs for individual interferograms of track D48 on the Tibetan Plateau (scaling factor = 0.9)

GIM	High-quality	Moderate-quality	Low-quality
jplg	9.50%	64.00%	26.50%
codg	6.00%	64.50%	29.50%
esag	3.00%	63.50%	33.50%
igsg	3.50%	69.00%	27.50%
emrg	0.50%	51.50%	48.00%
upcg	1.50%	51.00%	47.50%
uqrg	1.50%	40.00%	58.50%
casg	2.50%	61.00%	36.50%
jpld	11.50%	57.00%	31.50%

0% 100%

Table S5 Proportions of high-, moderate-, and low-quality ionospheric estimates derived from GIMs for individual interferograms of track A12 on the Tibetan Plateau (scaling factor = 0.9)

GIM	High-quality	Moderate-quality	Low-quality
jplg	5.50%	67.00%	27.50%
codg	5.50%	65.50%	29.00%
esag	6.50%	63.50%	30.00%
igsg	6.00%	64.00%	30.00%
emrg	5.50%	58.50%	36.00%
upcg	5.50%	63.50%	31.00%
uqrg	2.00%	62.00%	36.00%
casg	1.50%	65.50%	33.00%
jpld	6.50%	65.00%	28.50%

0% 100%

Table S6 Proportions of high-, moderate-, and low-quality ionospheric estimates derived from GIMs for individual interferograms of track D121 on the Tibetan Plateau (scaling factor = 0.9)

GIM	High-quality	Moderate-quality	Low-quality
jplg	5.00%	58.50%	36.50%
codg	3.00%	59.00%	38.00%
esag	2.00%	51.50%	46.50%
igsg	3.00%	57.50%	39.50%
emrg	0.50%	43.00%	56.50%
upcg	1.50%	43.50%	55.00%
uqrg	1.00%	33.50%	65.50%
casg	3.00%	41.00%	56.00%
jpld	5.50%	52.50%	42.00%

0% 100%

Table S7 RMS between CGPS velocities and InSAR velocities after correction using the range split-spectrum method and GIMs with different scaling factors. The unit is mm/yr. The data are from track A149 in northern Chile

No correction	Range split-spectrum method	GIM	Scaling factor					
			0.5	0.6	0.7	0.8	0.9	1.0
3.43	2.07	jplg	3.64	3.73	3.83	3.94	4.06	4.20
		codg	3.27	3.28	3.30	3.34	3.38	3.45
		esag	4.02	4.20	4.39	4.60	4.81	5.04
		igsg	4.03	4.20	4.37	4.56	4.75	4.96
		emrg	3.67	3.76	3.86	3.97	4.09	4.23
		upcg	4.14	4.33	4.52	4.73	4.94	5.16
		uqrg	3.05	3.06	3.09	3.15	3.24	3.35
		casg	3.51	3.56	3.62	3.69	3.77	3.86
		jpld	2.89	2.84	2.83	2.84	2.87	2.93

1 9
RMS (mm/yr)

Table S8 RMS between CGPS velocities and InSAR velocities after correction using the range split-spectrum method and GIMs with different scaling factors. The unit is mm/yr. The data are from track D156 in northern Chile

No correction	Range split-spectrum method	GIM	Scaling factor					
			0.5	0.6	0.7	0.8	0.9	1.0
1.97	1.39	jplg	1.86	1.85	1.85	1.85	1.85	1.86
		codg	1.73	1.70	1.69	1.68	1.68	1.69
		esag	1.67	1.63	1.60	1.58	1.57	1.57
		igsg	1.71	1.69	1.67	1.66	1.66	1.68
		emrg						
		upcg	1.66	1.63	1.62	1.62	1.63	1.66
		uqrg	1.58	1.55	1.54	1.55	1.58	1.62
		casg	1.83	1.81	1.80	1.79	1.79	1.79
		jpld	1.71	1.74	1.68	1.67	1.66	1.65

1 9
RMS (mm/yr)

Table S9 RMS between CGPS velocities and InSAR velocities after correction using the range split-spectrum method and GIMs with different scaling factors. The unit is mm/yr. The data are from track D48 on the Tibetan Plateau

No correction	Range split-spectrum method	GIM	Scaling factor					
			0.5	0.6	0.7	0.8	0.9	1.0
1.64	1.70	jplg	1.53	1.55	1.57	1.61	1.66	1.71
		codg	2.24	2.43	2.64	2.86	3.09	3.32
		esag	1.74	1.83	1.92	2.04	2.16	2.29
		igsg	1.77	1.84	1.92	2.00	2.10	2.20
		emrg	1.60	1.80	2.04	2.31	2.60	2.90
		upcg	1.77	1.83	1.91	1.99	2.08	2.18
		uqrg	2.18	2.34	2.52	2.71	2.90	3.10
		casg	2.01	2.15	2.30	2.47	2.64	2.82
		jpld	1.36	1.37	1.40	1.45	1.52	1.60

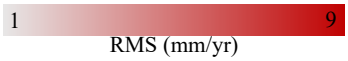

RMS (mm/yr)

Table S10 RMS between CGPS velocities and InSAR velocities after correction using the range split-spectrum method and GIMs with different scaling factors. The unit is mm/yr. The data are from track A12 on the Tibetan Plateau

No correction	Range split-spectrum method	GIM	Scaling factor					
			0.5	0.6	0.7	0.8	0.9	1.0
6.81	2.03	jplg	2.33	2.08	2.37	3.04	3.91	4.87
		codg	3.15	2.64	2.33	2.31	2.59	3.09
		esag	3.37	2.85	2.47	2.31	2.42	2.76
		igsg	3.71	3.16	2.68	2.30	2.08	2.08
		emrg	3.88	3.40	2.99	2.71	2.57	2.62
		upcg	4.39	3.93	3.49	3.08	2.70	2.38
		uqrg	5.44	5.18	4.91	4.65	4.40	4.15
		casg	2.90	2.41	2.20	2.36	2.81	3.45
		jpld	2.05	1.87	2.31	3.12	4.09	5.13

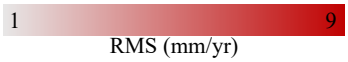

RMS (mm/yr)

Table S11 RMS between CGPS velocities and InSAR velocities after correction using the range split-spectrum method and GIMs with different scaling factors. The unit is mm/yr. The data are from track D121 on the Tibetan Plateau

No correction	Range split-spectrum method	GIM	Scaling factor					
			0.5	0.6	0.7	0.8	0.9	1.0
1.94	1.48	jplg	1.91	1.94	1.98	2.04	2.10	2.17
		codg	1.63	1.61	1.62	1.64	1.67	1.73
		esag	2.06	2.15	2.26	2.38	2.53	2.67
		igsg	1.74	1.72	1.71	1.70	1.71	1.72
		emrg	3.09	3.43	3.79	4.17	4.55	4.94
		upcg	1.94	1.96	1.99	2.03	2.07	2.12
		uqrg	1.84	1.85	1.88	1.92	1.97	2.03
		casg	1.77	1.78	1.79	1.82	1.86	1.92
		jpld	2.18	2.28	2.40	2.53	2.67	2.81

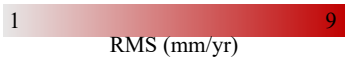

RMS (mm/yr)

Table S12 RMS between CGPS velocities and InSAR velocities after correction using GIMs with different empirical adaptive scaling factors

Track	A149				A149_half_cycle				A41				A12			
Scaling factor	Long-term		Seasonal		Long-term		Seasonal		Long-term		Seasonal		Long-term		Seasonal	
	poly	sin	poly	sin	poly	sin	poly	sin	poly	sin	poly	sin	poly	sin	poly	sin
Corrected by codg	3.17	3.15	3.99	3.81	4.95	5.25	5.87	5.79	2.57	2.51	6.33	7.11	2.28	2.27	3.95	4.05
Corrected by jplg	3.79	3.81	4.74	4.61	5.23	5.37	6.47	6.38	3.24	3.24	6.92	7.76	2.61	2.74	6.22	6.34
Corrected by jpld	2.77	2.59	3.71	3.76	4.31	4.22	6.14	6.03	4.40	4.41	7.43	8.20	2.58	2.76	6.47	6.74
Corredted by uqrg	2.79	2.80	4.04	3.83	2.78	2.85	5.66	5.27	5.94	5.59	3.61	3.08	5.44	5.31	4.03	3.92

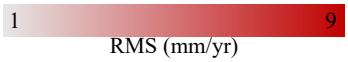

RMS (mm/yr)

Table S13 RMS of mean deformation velocities of time series with different time spans relative to the solar cycle. The data are from track D156 in northern Chile

Period ratio	Start date	End date	Number of dates	No correction	Corrected by range split-spectrum method	Corrected by codg with a scaling factor 0.9	Corrected by GIMs with an empirical adaptive scaling factor			
							codg	jplg	jpld	uqrg
1:1	20160929	20230303	171	1.96	1.54	1.79	1.71	1.91	1.75	1.84
	20170328	20220904	149	1.66	1.64	1.69	1.67	1.79	1.72	1.70
	20171006	20220224	122	1.73	1.73	1.73	1.71	1.79	1.78	2.13
	20180428	20210729	92	1.98	2.05	1.99	2.02	2.09	2.00	2.44
	20190117	20201107	54	3.30	2.97	3.40	3.44	3.02	3.00	3.01
1:2	20180428	20230327	132	3.47	1.86	2.45	2.35	2.70	2.44	2.66
	20180814	20220811	110	2.22	2.16	2.39	2.41	2.25	2.35	2.58
	20181106	20220224	95	2.47	2.42	2.60	2.63	2.47	2.58	3.56
	20190222	20210729	73	2.71	2.55	2.81	2.80	2.52	2.55	3.49
	20190529	20210118	49	3.22	3.74	3.82	4.03	3.84	4.07	9.43
2:1	20150613	20220320	160	1.48	1.41	1.45	1.47	1.59	1.49	1.47
	20161011	20210717	131	1.56	1.57	1.51	1.51	1.62	1.52	1.67
	20171006	20210118	93	1.57	1.41	1.52	1.50	1.50	1.43	1.82
	20180416	20201014	69	2.29	2.38	2.24	2.24	2.44	2.24	2.10
	20181106	20200710	50	3.05	3.29	3.05	3.25	2.98	2.91	3.57

	20150426	20191219	98	1.57	1.18	1.25	1.40	1.57	1.43	2.13
other	20191219	20230327	89	6.02	2.03	3.40	3.34	3.54	3.29	4.17
	20150426	20230327	186	1.97	1.39	1.68	1.64	1.86	1.65	1.55

40 200 Number of Dates

1 9 RMS (mm/yr)

Table S14 RMS of mean deformation velocities of time series with different time spans relative to the solar cycle. The data are from track A41 on the Tibetan Plateau

Period ratio	Start date	End date	Number of dates	No correction	Corrected by range split-spectrum method	Corrected by codg with a scaling factor 0.9	Corrected by GIMs with an empirical adaptive scaling factor			
							codg	jplg	jpld	uqrg
	20151214	20231208	215	11.27	1.94	5.32	3.05	3.71	5.18	7.03
	20170101	20221119	172	7.36	1.96	5.12	3.95	4.25	5.25	5.55
1:1	20171004	20220228	133	3.98	2.11	3.09	2.56	2.99	3.96	4.12
	20180613	20210621	93	6.03	2.49	2.63	2.90	3.01	3.55	3.42
	20190220	20201012	51	10.58	3.64	5.11	5.82	5.21	4.82	5.55
	20171215	20231208	176	17.58	2.15	9.29	4.67	4.95	7.23	10.42
	20180414	20230412	149	15.05	2.14	8.65	4.95	5.33	7.26	9.32
1:2	20180731	20220920	125	11.13	2.30	7.53	5.53	5.85	7.13	6.73
	20181104	20220312	103	5.54	2.40	6.95	5.92	7.90	8.29	4.51
	20190220	20210808	76	6.40	2.58	3.17	4.51	3.11	3.10	4.05
	20150512	20220405	178	1.85	1.86	1.71	1.78	2.31	2.75	1.87
	20160530	20210925	147	2.36	2.10	2.37	2.15	2.23	2.17	2.77
2:1	20170314	20210504	123	2.96	2.39	2.45	2.34	3.00	3.03	2.99
	20171004	20210116	99	3.47	2.33	2.70	2.89	2.94	2.65	3.97
	20180426	20201012	75	6.15	2.81	3.89	4.04	4.14	3.36	4.93
	20150512	20191217	108	7.08	2.20	6.64	4.09	3.71	2.85	4.13
other	20191217	20231208	117	29.59	2.88	14.96	6.50	7.00	10.76	17.42
	20150512	20231208	224	9.16	1.89	4.16	2.51	3.24	4.41	5.59

40 200 Number of Dates

1 9 RMS (mm/yr)

Table S15 RMS of mean deformation velocities of time series with different time spans relative to the solar cycle. The data are from track D48 on the Tibetan Plateau

Period ratio	Start date	End date	Number of dates	No correction	Corrected by range split-spectrum method	Corrected by codg with a scaling factor 0.9	Corrected by GIMs with an empirical adaptive scaling factor			
							codg	jplg	jpld	uqrg
	20170407	20220827	134	1.54	1.53	2.11	1.84	1.75	1.52	2.47
	20171109	20220123	106	1.80	1.62	1.79	1.82	1.81	1.80	1.90
1:1	20180719	20210516	71	2.10	2.03	2.33	2.51	2.35	2.18	3.42
	20181104	20210128	56	2.64	2.27	2.55	2.59	2.88	3.04	4.43
	20190220	20201012	39	2.72	2.55	3.94	5.09	2.71	2.70	4.18
	20171227	20231126	147	1.78	1.83	3.75	2.71	1.46	1.45	2.31
	20180613	20221225	115	1.74	1.87	3.82	3.11	1.65	1.48	2.12
1:2	20181023	20220324	88	1.76	1.82	3.04	2.83	2.03	1.94	2.00
	20190127	20210925	67	2.36	2.03	2.29	2.56	2.82	2.27	3.03
	20190421	20210329	48	3.06	3.38	2.74	3.00	6.10	3.09	3.01
	20170326	20210422	100	1.79	1.56	1.81	1.90	2.11	1.71	3.36
	20170525	20210329	94	1.86	1.65	1.80	1.87	2.01	1.85	3.68
2:1	20170910	20210128	84	1.94	1.72	2.02	2.10	2.09	1.87	3.93
	20180309	20201105	65	2.30	2.03	2.24	2.30	2.68	2.15	5.12
	20180905	20200801	48	3.74	2.66	3.08	3.04	3.79	2.70	6.41
	20170326	20191217	64	2.23	1.76	2.12	2.28	4.35	2.40	3.93
other	20191217	20231126	101	2.99	2.73	6.81	5.15	1.64	1.50	2.81
	20170326	20231126	164	1.64	1.70	3.09	2.30	1.42	1.35	2.62

40 200 Number of Dates

1 9 RMS (mm/yr)

Table S16 RMS of mean deformation velocities of time series with different time spans relative to the solar cycle. The data are from track A12 on the Tibetan Plateau

Period ratio	Start date	End date	Number of dates	No correction	Corrected by range split-spectrum method	Corrected by codg with a scaling factor 0.9	Corrected by GIMs with an empirical adaptive scaling factor			
							codg	jplg	jpld	uqrg
	20160925	20230305	183	9.42	2.17	3.60	2.69	3.33	3.40	6.59
	20170312	20220918	161	7.48	2.18	2.56	2.19	2.85	3.31	4.85
1:1	20171119	20220109	122	3.50	2.10	3.39	2.97	3.84	5.54	4.75
	20180729	20210502	82	3.05	2.14	4.15	4.23	4.59	5.89	3.29
	20190218	20201010	49	3.75	3.45	4.08	6.02	9.80	8.80	12.55
	20180506	20230305	142	14.13	2.22	7.23	4.43	5.74	6.00	9.00
	20180729	20220918	121	12.06	2.18	5.74	4.02	5.93	6.70	6.10
1:2	20181102	20220310	98	5.15	2.31	9.10	8.21	10.08	12.18	6.22
	20190218	20210806	74	2.76	2.35	4.33	3.05	2.60	3.10	5.18
	20190513	20210219	53	9.90	2.75	6.79	5.07	3.69	5.56	3.48
2:1	20150721	20220226	164	1.99	2.03	1.92	1.76	2.16	2.64	2.70
	20160808	20210818	140	2.43	2.27	3.28	3.32	2.33	2.07	3.39

	20170920	20210126	99	4.25	2.36	4.66	5.02	4.71	3.37	5.27
	20180424	20201010	73	5.57	2.56	4.77	4.99	6.13	3.35	7.62
	20181102	20200706	49	9.26	3.49	4.49	7.03	5.18	9.32	7.96
	20150721	20191215	100	5.87	2.38	7.56	5.45	3.24	3.95	2.60
other	20191215	20230317	96	25.76	2.88	12.41	6.68	9.10	7.92	14.57
	20151721	20230317	195	6.81	2.03	2.59	2.27	2.74	2.76	5.31

40 200 Number of Dates

1 9 RMS (mm/yr)

Table S17 RMS of mean deformation velocities of time series with different time spans relative to the solar cycle. The data are from track D121 on the Tibetan Plateau

Period ratio	Start date	End date	Number of dates	No correction	Corrected by range split-spectrum method	Corrected by codg with a scaling factor 0.9	Corrected by GIMs with an empirical adaptive scaling factor			
							codg	jplg	jpld	uqrg
	20170413	20220821	151	1.73	1.37	1.53	1.57	1.51	1.59	1.72
	20180114	20211118	111	1.51	1.48	1.43	1.46	1.59	1.51	2.13
1:1	20180526	20210709	89	1.54	1.68	1.61	1.57	1.73	1.86	2.18
	20181017	20210215	69	1.70	1.71	1.66	1.67	2.04	1.88	2.12
	20190226	20201006	45	2.83	2.67	2.82	2.98	2.59	2.71	3.34
	20170413	20210416	113	1.29	1.39	1.41	1.49	1.63	1.43	2.46
	20170904	20210203	98	1.26	1.26	1.30	1.33	1.61	1.33	3.58
1:2	20180126	20201123	81	1.25	1.26	1.24	1.27	1.68	1.36	4.64
	20180713	20200831	60	1.30	1.51	1.50	1.72	3.32	2.20	5.28
	20181110	20200702	46	1.93	1.60	2.25	2.48	2.70	2.31	3.51
	20180102	20231108	166	2.18	1.55	1.74	1.66	2.45	2.64	2.42
	20180619	20221207	128	2.19	1.55	1.72	1.62	2.31	2.61	2.76
2:1	20181110	20220222	93	1.99	1.66	1.63	1.60	2.05	2.14	2.78
	20190214	20210814	73	2.22	2.23	2.14	2.11	2.03	2.09	3.05
	20190614	20201217	45	3.76	2.95	2.75	2.76	3.77	4.40	3.31
	20170413	20191211	74	1.68	1.69	2.10	2.13	2.87	2.13	3.90
other	20191211	20231120	112	3.14	2.09	2.26	2.07	4.32	4.52	4.50
	20170413	20231120	185	1.94	1.48	1.67	1.63	1.99	2.29	2.05

40 200 Number of Dates

1 9 RMS (mm/yr)

2 Figures

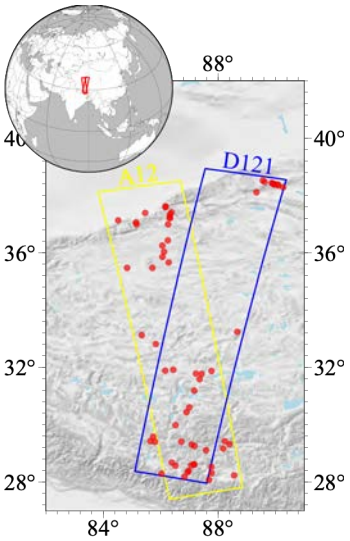

Fig. S1 Coverage of Sentinel-1 SAR data for tracks A12 and D121 on the Tibetan Plateau. Red dots denote CGPS stations used to validate InSAR measurements

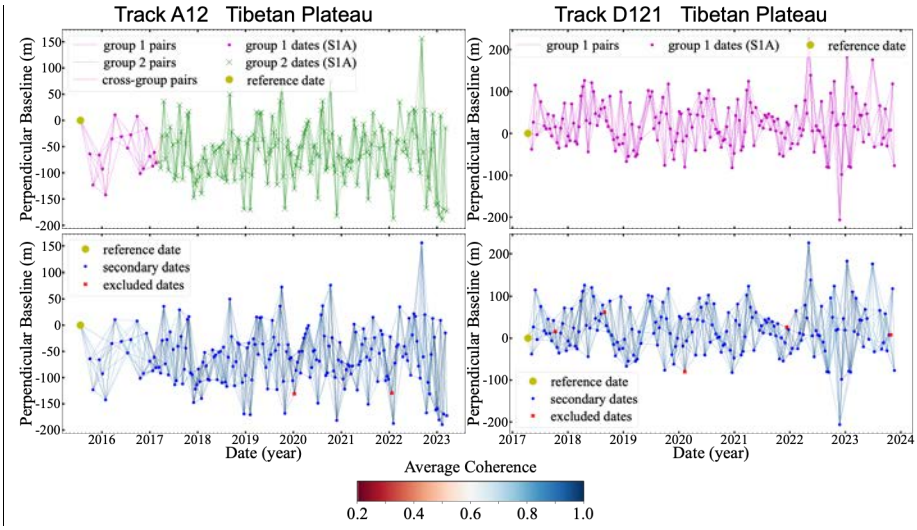

Fig. S2 Networks of InSAR stacks for tracks A12 and D121 on the Tibetan Plateau. In each panel, the upper plot shows the ionospheric phase estimation network with the range split-spectrum method, while the lower plot shows the InSAR network for time series analysis. In the lower plots, acquisitions marked by red crosses are excluded because of missing GIMs as also shown in Table 1. The colors of the lines connecting the dates represent mean coherence of interferometric pairs. The high coherence enables reliable estimation of ionospheric phase using the range split-spectrum method

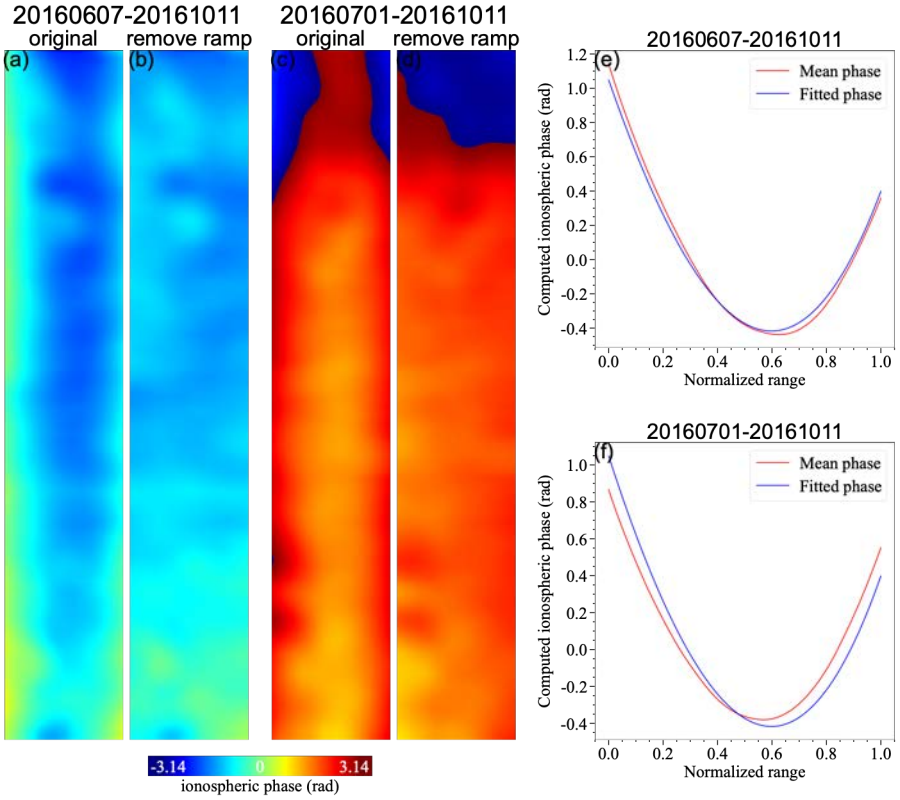

Fig. S3 Two examples of ionospheric phase estimation with the range split-spectrum method for cross-satellite pairs. The range ramps in the original estimates are clear and removed using the empirical formula given in Eq. (S1). (a) Original ionospheric phase estimate of pair 20160607 (S1A) - 20161011 (S1B). (c) Original ionospheric phase estimate of pair 20160701 (S1A) - 20161011 (S1B). (b) and (d) Ionospheric phases in (a) and (c) after removing the range ramp with Eq. (S1). (e) and (f) Original phase profile (mean of all lines) and the fitted phase (computed by Eq. (S1)) of the two pairs. The examples are from track D156 in northern Chile

$$\emptyset_{\text{ion,ramp}} = 1.05 - 4.56r + 2.96r^2 + 0.95r^3 \quad \text{(S1)}$$

where $0 \leq r \leq 1$ is the normalized range. Note that the equation is for descending S1A-S1B pairs. For ascending S1A-S1B pairs, it should be flipped in range. For S1B-S1A pairs, the sign should be changed

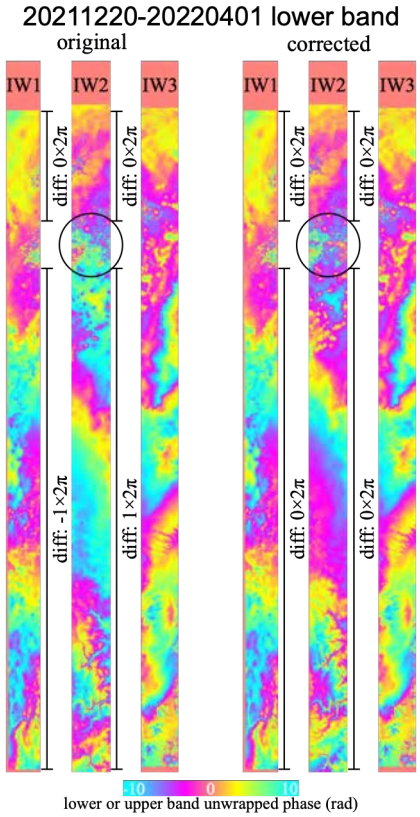

Fig. S4 An example of correction of unwrapping errors in cross-group sub-band interferograms. The example is from track D156 in northern Chile. The reported phase differences are the mean values within the overlap regions (swath2-swath1, swath3-swath2)

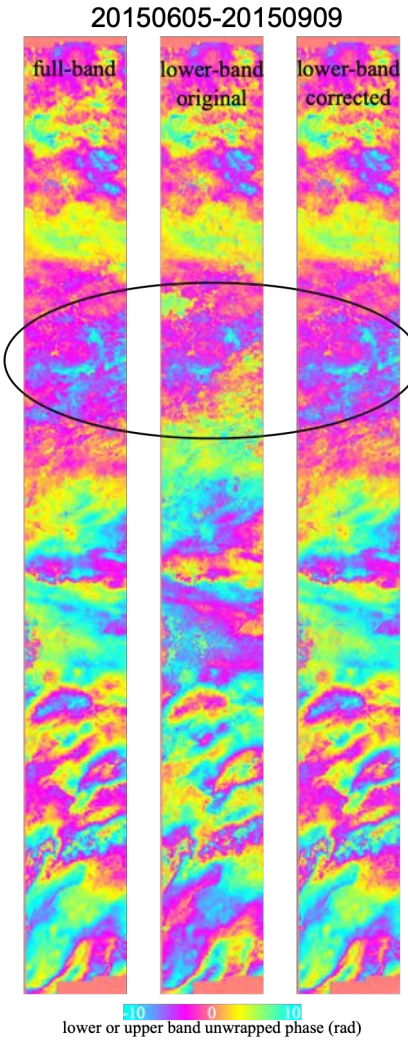

Fig. S5 An example of correction of unwrapping errors in same-group sub-band interferograms. The example is from track A41 on the Tibetan Plateau

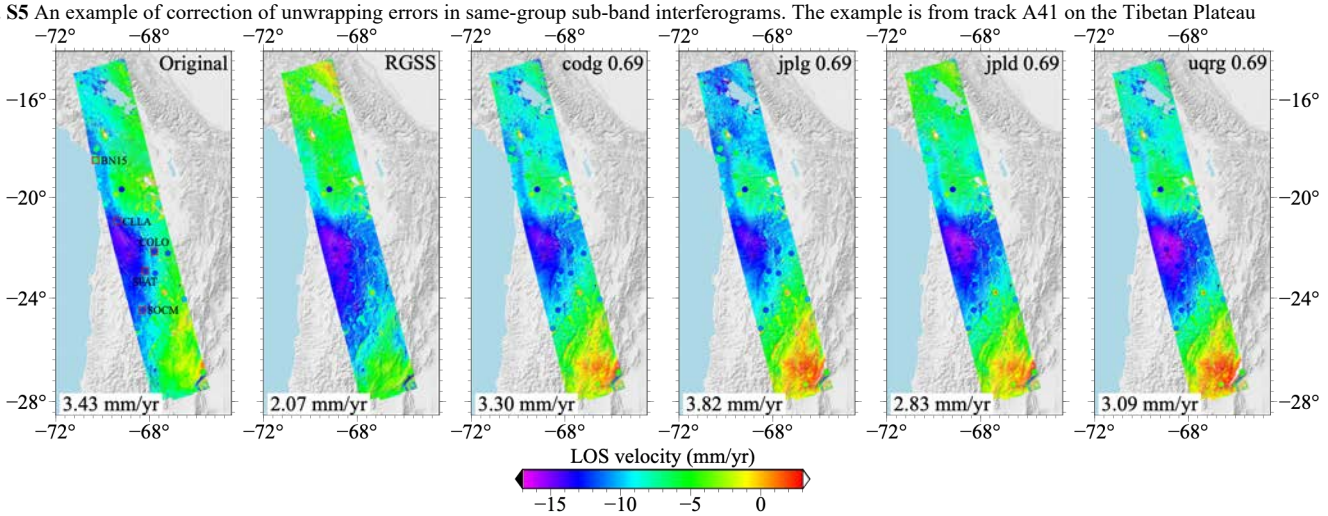

Fig. S6 Mean deformation velocities of track A149 in northern Chile, with and without ionospheric corrections. A scaling factor of 0.69 is used in the correction with GIMs. The circles represent the locations of CGPS stations, with colors denoting the mean velocity measured by CGPS projected to the InSAR LOS direction

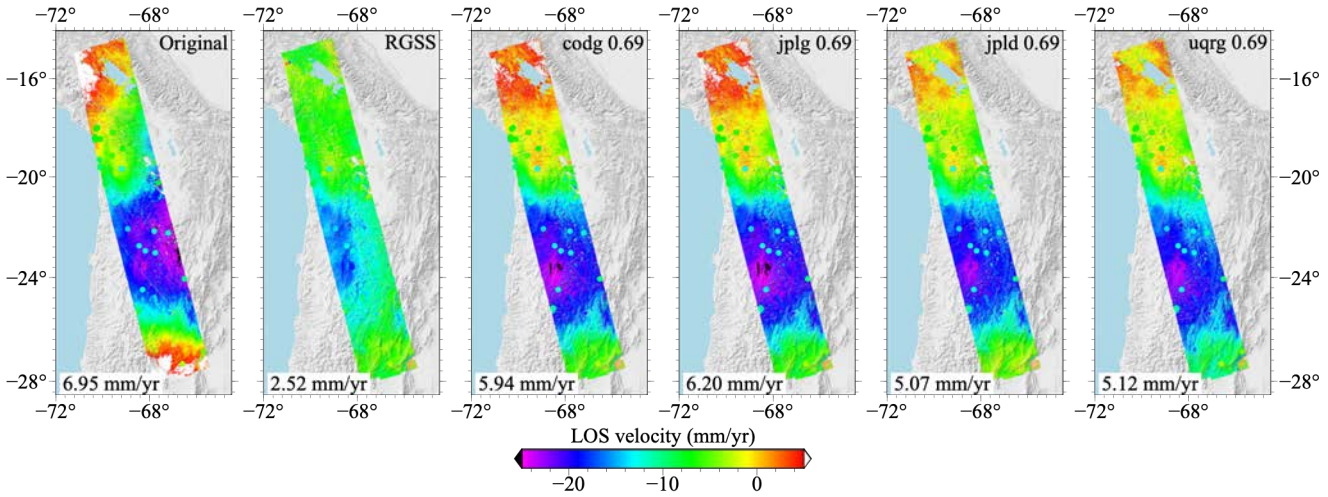

Fig. S7 Mean deformation velocities of track A149 in northern Chile, spanning the second half of solar cycle 24, with and without ionospheric corrections. A scaling factor of 0.69 is used in the correction with GIMs. The circles represent the locations of CGPS stations, with colors denoting mean velocity measured by CGPS projected to the InSAR LOS direction

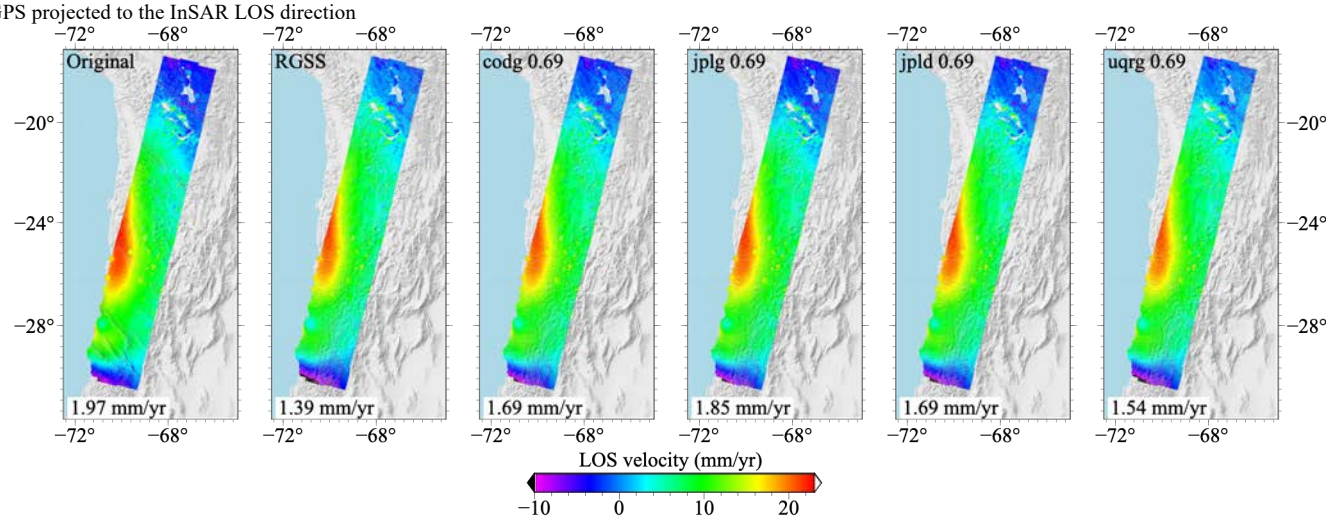

Fig. S8 Mean deformation velocities of track D156 in northern Chile, with and without ionospheric corrections. A scaling factor of 0.69 is used in the correction with GIMs. The circles represent the locations of CGPS stations, with colors denoting mean velocity measured by CGPS projected to the InSAR LOS direction

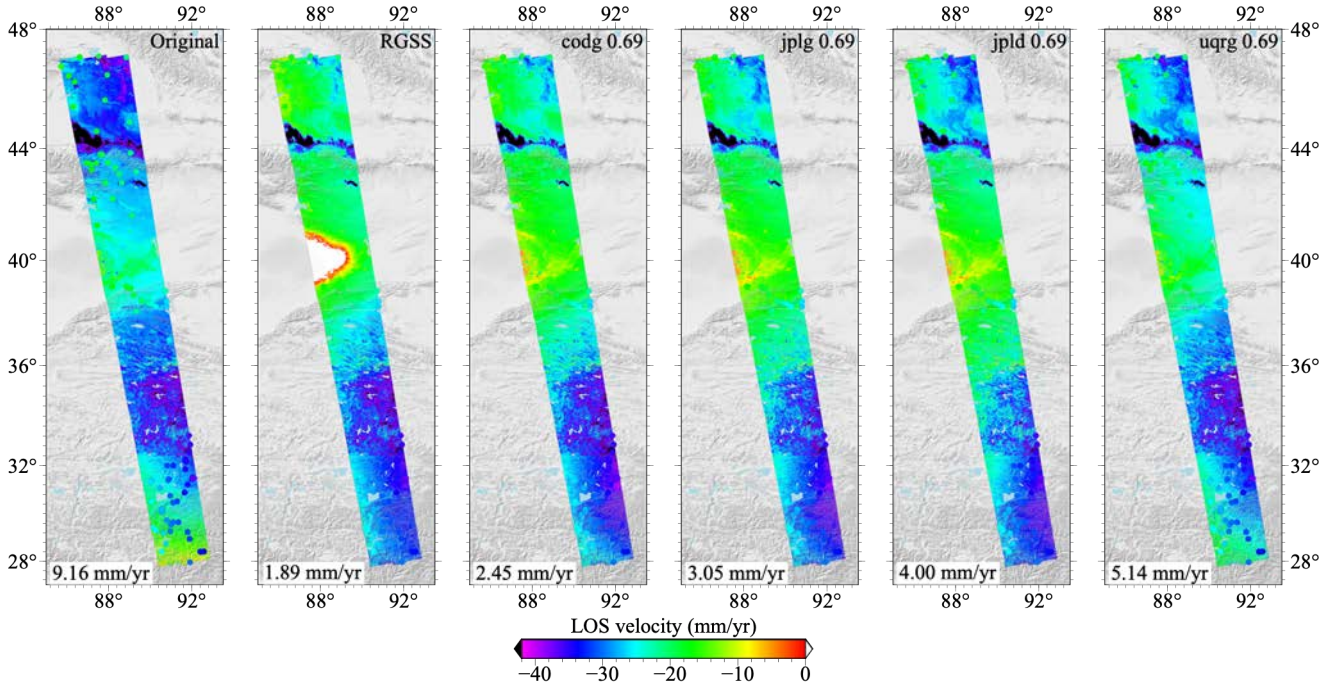

Fig. S9 Mean deformation velocities of track A41 on the Tibetan Plateau, with and without ionospheric corrections. A scaling factor of 0.69 is used in the correction with GIMs. The circles represent the locations of CGPS stations, with colors denoting mean velocity measured by CGPS projected to the InSAR LOS direction

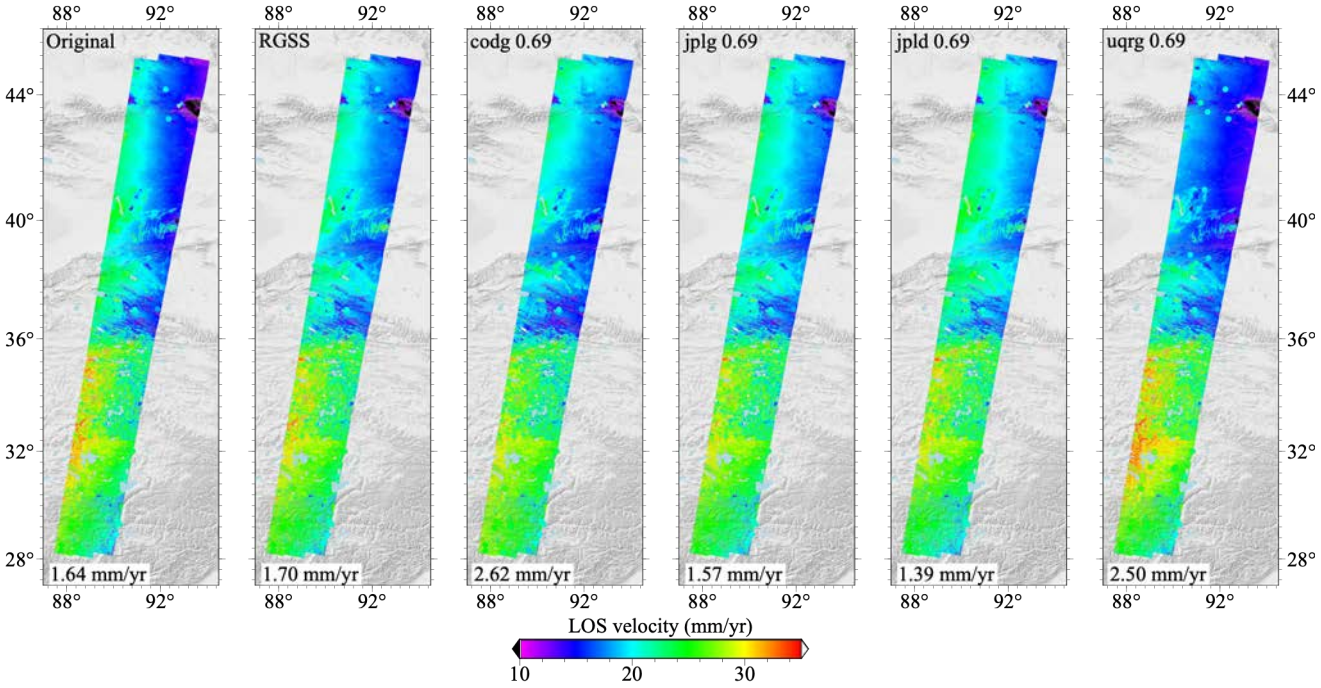

Fig. S10 Mean deformation velocities of track D48 on the Tibetan Plateau, with and without ionospheric corrections. A scaling factor of 0.69 is used in the correction with GIMs. The circles represent the locations of CGPS stations, with colors denoting mean velocity measured by CGPS projected to the InSAR LOS direction

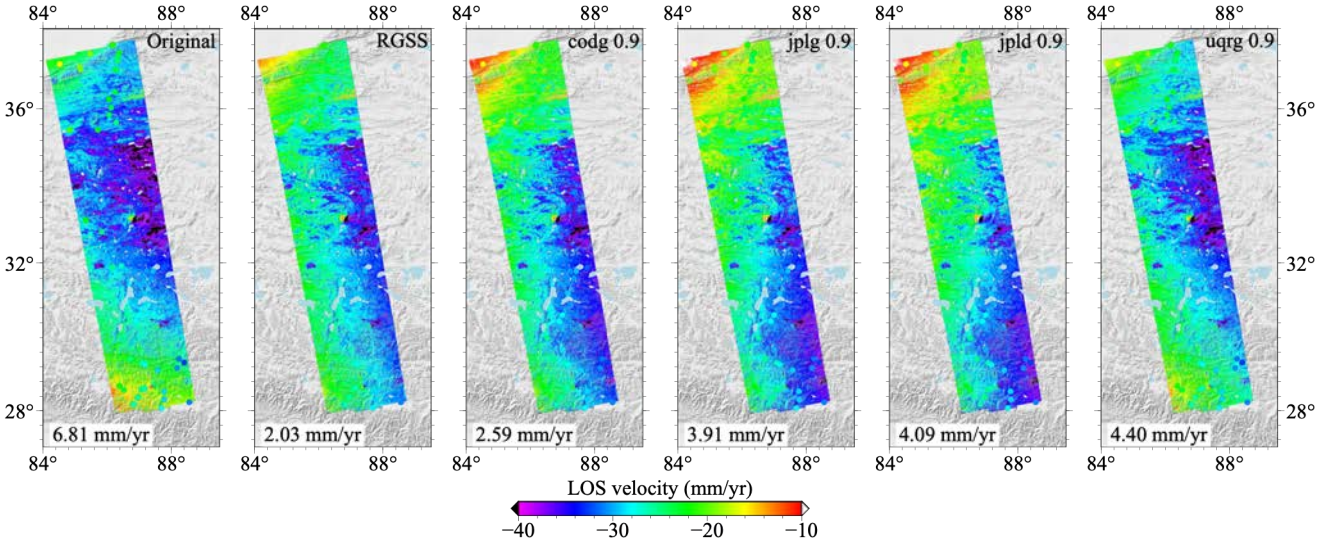

Fig. S11 Mean deformation velocities of track A12 on the Tibetan Plateau, with and without ionospheric corrections. A scaling factor of 0.9 is used in the correction with GIMs. The circles represent the locations of CGPS stations, with colors denoting mean velocity measured by CGPS projected to the InSAR LOS direction

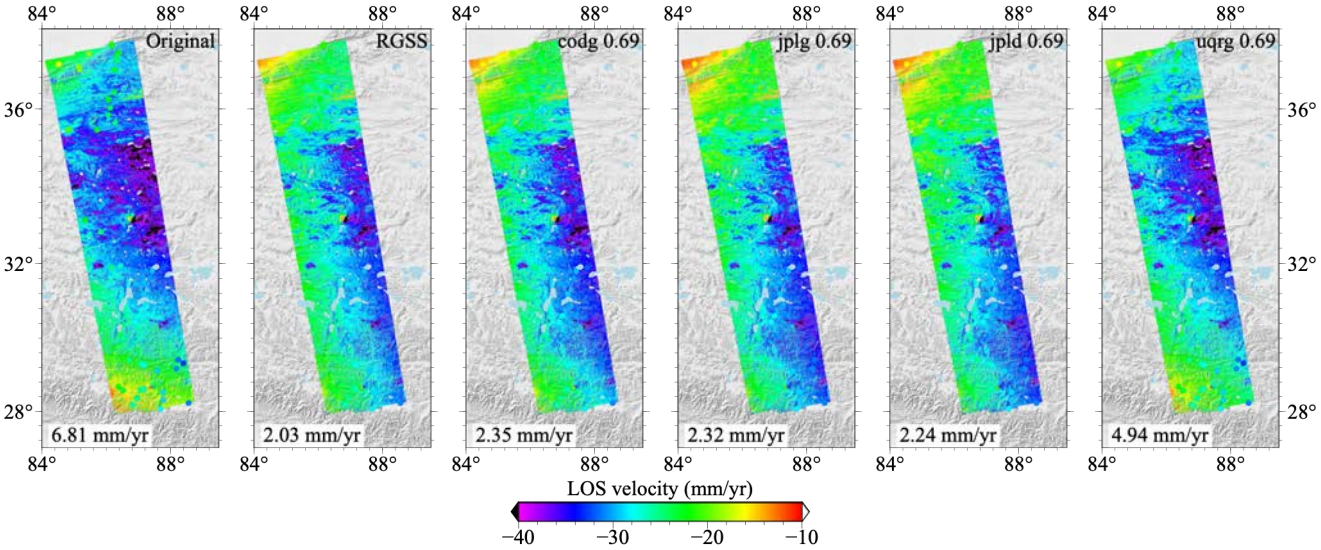

Fig. S12 Mean deformation velocities of track A12 on the Tibetan Plateau, with and without ionospheric corrections. A scaling factor of 0.69 is used in the correction with GIMs. The circles represent the locations of CGPS stations, with colors denoting mean velocity measured by CGPS projected to the InSAR LOS direction

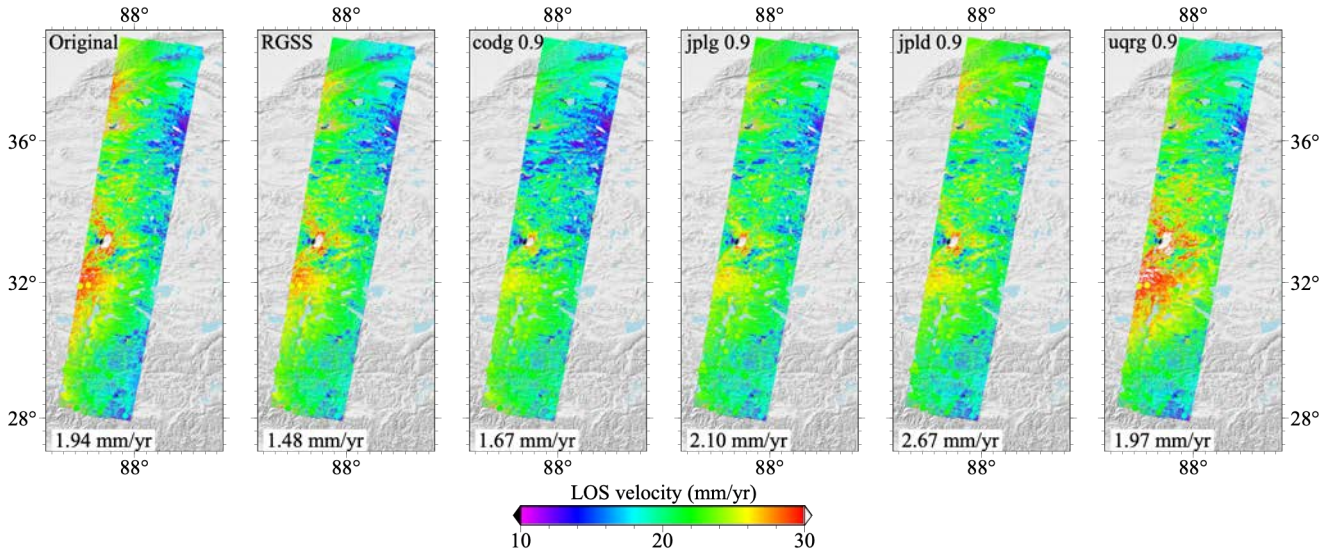

Fig. S13 Mean deformation velocities of track D121 on the Tibetan Plateau, with and without ionospheric corrections. A scaling factor of 0.9 is used in the correction with GIMs. The circles represent the locations of CGPS stations, with colors denoting mean velocity measured by CGPS projected to the InSAR LOS direction

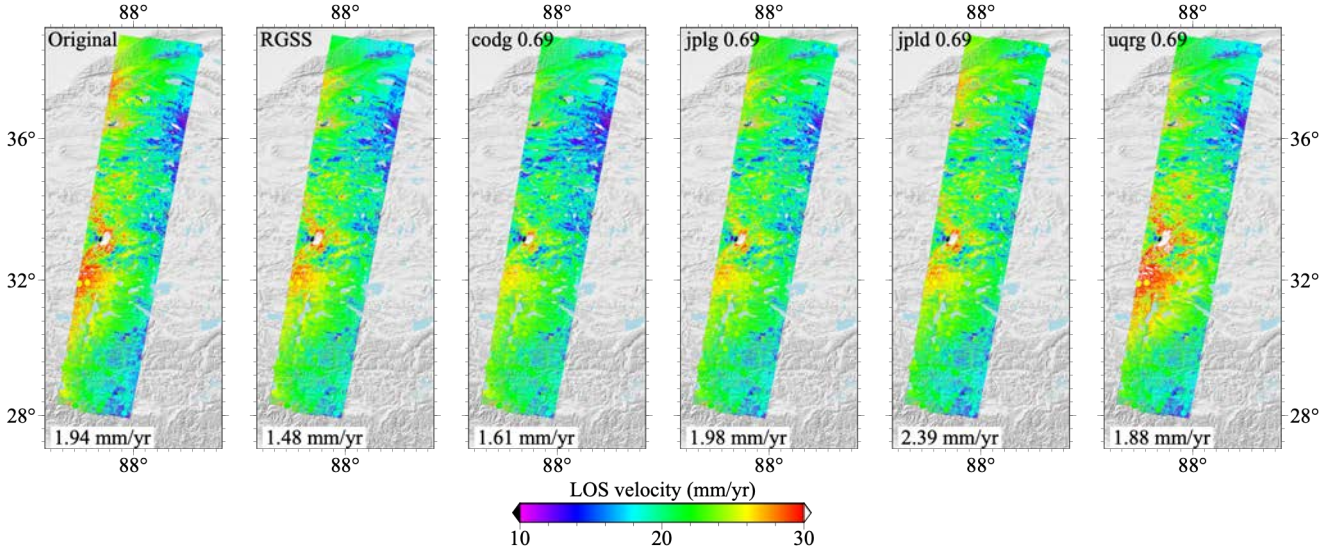

Fig. S14 Mean deformation velocities of track D121 on the Tibetan Plateau, with and without ionospheric corrections. A scaling factor of 0.69 is used in the correction with GIMs. The circles represent the locations of CGPS stations, with colors denoting mean velocity measured by CGPS projected to the InSAR LOS direction

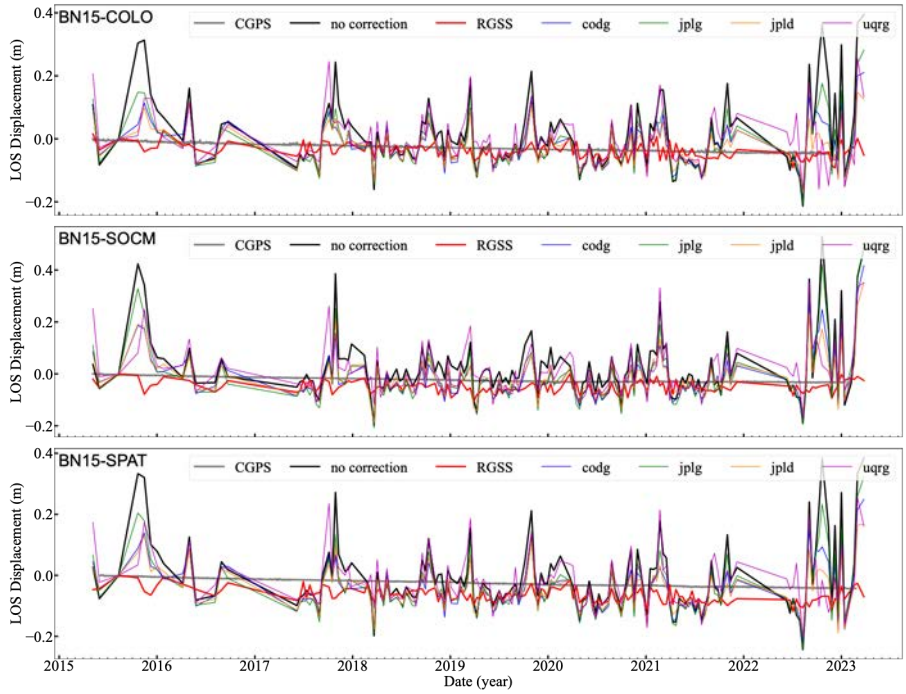

Fig. S15 Deformation time series of track A149 in northern Chile, from CGPS (COLO, SOCM and SPAT) and InSAR with and without ionospheric corrections. A scaling factor of 0.9 is used in the correction with GIMs

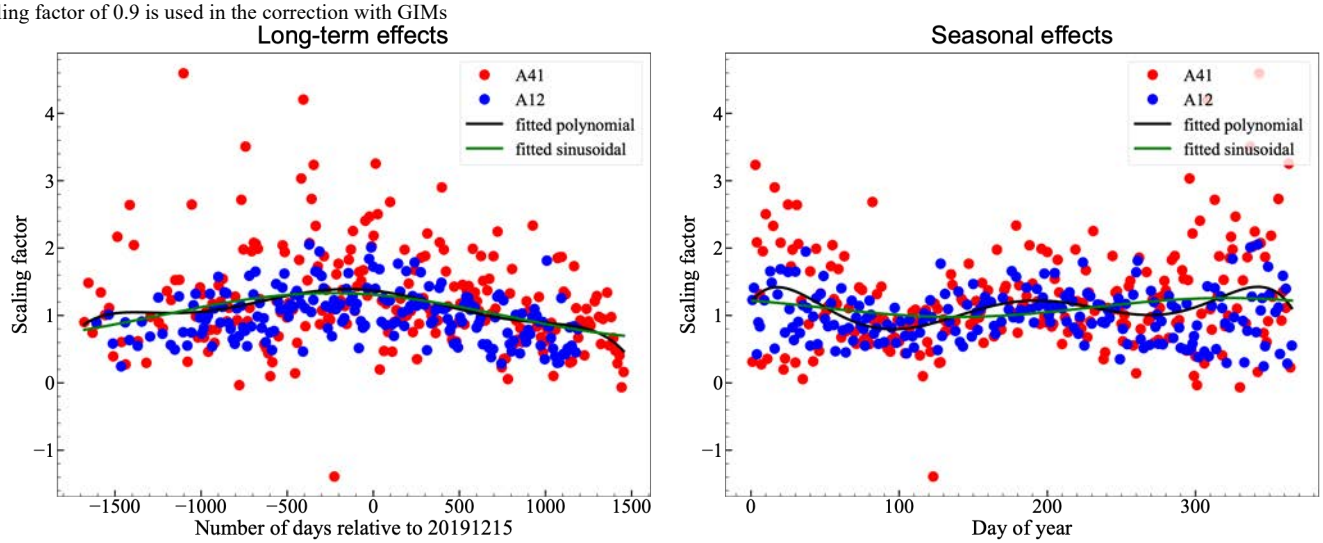

Fig. S16 Empirical adaptive scaling factor accounting for long-term effects (solar cycle) and seasonal effects computed using ionospheric phases estimated by the range split-spectrum method and codg GIMs. Tracks A41 and A12 on the Tibetan Plateau are used

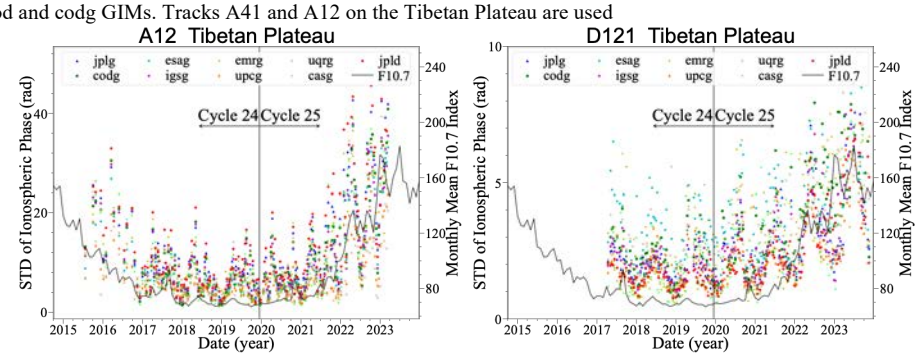

Fig. S17 Comparison of F10.7 index and spatial standard deviation of ionospheric phases from GIMs for tracks A12 and D121 on the Tibetan Plateau

3 Identification and correction of unwrapping errors in sub-band interferograms

After obtaining the ionospheric phase using the topsStack workflow in ISCE2, we perform a systematic quality check of both the sub-band interferograms and the preliminary ionospheric phase estimates. For each pair, we compare the ionospheric phase, the lower- and upper-band interferograms, and the full-band interferogram. We then rewrap the unwrapped interferograms into the range of -10 to 10 radians, and rewrap the filtered ionospheric phase into the range of $-\pi$ to π radians. Unwrapping errors can then be identified based on the following characteristics:

1) Ionospheric phase characteristics. The ionospheric phase is expected to exhibit long-wavelength variations. If abnormally dense fringes appear in the ionospheric phase estimate, this is a strong indicator of unwrapping errors. However, when identical unwrapping errors occur in both the lower- and upper-band interferograms , there are no dense fringes in the ionospheric phase estimate. The resulting errors instead manifest as subtle but abnormal fringe patterns in the ionospheric phase estimate, such as the left-panel example (20211220-20220401 of track D156 in northern Chile) shown in Fig. 7.

2) Comparison between sub-band and full-band interferograms. Unwrapping errors occur more frequently in sub-band interferograms because of their higher noise level. If a sub-band interferogram shows fringe patterns that differ markedly from the corresponding full-band interferogram, or if the lower- and upper-band interferograms exhibit substantially different fringe patterns, unwrapping errors are likely present.

3) Swath consistency for cross-group pairs. For cross-group pairs, we estimate the ionospheric phase swath by swath; consequently, the sub-band swath interferograms may be segmented into disconnected regions. When all three swaths are correctly unwrapped, the phase differences within the overlap regions between adjacent swaths should be consistent. If unwrapping errors occur in one swath, the phase difference in the overlap region containing the error will deviate from the expected pattern, as illustrated in Fig. S4.

As InSAR measurements are spatially relative, comparisons focus on fringe patterns rather than absolute phase values. Once unwrapping errors are identified, we correct them using the following procedures.

A. Cross-group pairs

We use the overlap regions between adjacent swaths to identify and correct unwrapping errors. These errors typically arise in areas of very low coherence that segment a swath into multiple disconnected regions. Fig. S4 shows such an example. The low coherence area (circled in Fig. S4) segments swath2 into two disconnected regions. We calculate the phase difference in the overlap region between adjacent swaths. The averaged phase differences are marked in Fig. S4. Because the unwrapped phase is spatially relative, we can adjust either the upper or lower part of the affected swath to resolve the inconsistency. In this example, we add $1 \times 2\pi$ to the lower part of swath2, which brings the phase differences in both overlap regions to zero, as shown in the right panel of Fig. S4. The low-coherence area itself is subsequently masked or filtered out during ionospheric phase smoothing. After this

adjustment, the unwrapping error is effectively corrected.

B. Same-group pairs

We use the correctly unwrapped full-band interferogram as a reference to correct unwrapping errors in the sub-band interferograms. The carrier frequency of Sentinel-1 is approximately 5.405 GHz and the 1/3 bandwidth used for split-spectrum processing is approximately 16.1 MHz (parameters from swath2 of track A41). According to $\Delta\varphi = \frac{4\pi\Delta f}{c} d$ (where $\Delta\varphi$ is the difference between full-band and sub-band interferogram phase, Δf is the difference of center frequency (here is 1/3 bandwidth), c is the speed of light, and d is the LOS displacement), when $d = 1$ meter, $\Delta\varphi = 0.3374$ radian. This implies that the integer number of phase cycles (the "wrapping number") remains almost consistently the same for the full-band and sub-band interferograms. Therefore, we can use the correctly unwrapped full-band interferogram to determine the required integer multiple of 2π to be added to each sub-band interferogram. Fig. S5 illustrates this correction procedure for a pair.

4 Detailed processing of GIMs

We first determine the Ionospheric Pierce Point (IPP) corresponding to each pixel in the multilooked interferogram. For a given pixel, we calculate its geographic coordinates (latitude, longitude and height) and convert them to geocentric Cartesian coordinates. We adopt the "stop-and-go" assumption, which implies that the satellite is stationary at an azimuth position when transmitting and receiving signal for a line and then moves to the next position for the next line; therefore, the radar position is identical for all pixels within the same azimuth line. Given an azimuth line, we calculate the radar position at zero Doppler time by interpolating the precise Sentinel-1 orbit data. Ideally, we should account for the azimuth beam steering in TOPS mode, rather than assuming a zero-Doppler geometry. Nevertheless, given the coarse spatial resolution of the GIMs, the error introduced by this simplification is negligible.

Given the image pixel and radar positions, we can calculate the IPP position by solving the following equations

$$\begin{cases} X_{\mathrm{IPP}} = X_g + s \cdot \dfrac{X_s - X_g}{|X_s - X_g|} \\ (H + R_B)^2 = |X_{\mathrm{IPP}}|^2 \end{cases} \tag{S2}$$

where X_{IPP}, X_s and X_g are the position vectors of IPP, radar and the target on the ground in geocentric Cartesian coordinate system, respectively, H is the height of the modeled ionosphere layer, R_B is the base radius of the Earth (as shown in Table 2), and s is the distance between IPP and target positions. Solving the equations yields two solutions of s, and the solution closer to the radar position X_s should be used.

Since GIMs are provided in geographic coordinates, we convert the geocentric Cartesian coordinates of X_{IPP} into latitude and longitude by

$$\begin{cases} \lambda_{\mathrm{IPP}} = arctan\dfrac{y_{\mathrm{IPP}}}{x_{\mathrm{IPP}}} \\ \phi_{\mathrm{IPP}} = arctan\dfrac{z_{\mathrm{IPP}}}{\sqrt{x_{\mathrm{IPP}}^2 + y_{\mathrm{IPP}}^2}} \end{cases} \tag{S3}$$

where λ_{IPP} and ϕ_{IPP} are the geocentric longitude and latitude of IPP, respectively, and $(x_{\mathrm{IPP}}, y_{\mathrm{IPP}}, z_{\mathrm{IPP}})$ are the Cartesian coordinates of IPP. Note that the latitude and longitude in GIMs are defined on the sphere of the ionosphere shell; therefore, iteration is not required here. This differs from the standard conversion from Cartesian coordinates to geodetic coordinates.

The SAR acquisition time generally differs from the GIM epoch. We follow the method recommended in IONEX format (Schaer and Gurtner, 1998)[1] to deal with this problem. We first find the two GIM epochs with times closest to the SAR acquisition time. For each of the GIM epochs, the longitude calculated earlier is adjusted to account for Earth's rotation

$$\lambda'_{\mathrm{IPP},k} = \lambda_{\mathrm{IPP}} + (t - T_k) \cdot \omega_e \tag{S4}$$

where $\lambda'_{\mathrm{IPP},k}$ is the adjusted longitude of the kth GIM epoth of the SAR acquisition date, t is the SAR acquisition time, T_k is the time of the kth GIMs, and ω_e is the Earth rotation constant and $\omega_e = 360°/24\mathrm{h}$.

Using the adjusted $\lambda'_{\mathrm{IPP},k}$ and ϕ_{IPP}, we spatially interpolate the two GIMs using a bicubic kernel to generate the VTEC values at $(\emptyset_{\mathrm{IPP}}, \lambda'_{\mathrm{IPP},i}, T_i)$ and $(\emptyset_{\mathrm{IPP}}, \lambda'_{\mathrm{IPP},i+1}, T_{i+1})$, where T_i and T_{i+1} are the times of the two GIMs. Then we temporally interpolate the two resulting VTEC using a simple linear kernel to obtain the VTEC matching SAR acquisition both spatially and temporally

$$VTEC_{\mathrm{IPP},t} = \frac{T_{i+1} - t}{T_{i+1} - T_i} VTEC\left(\emptyset_{\mathrm{IPP}}, \lambda'_{\mathrm{IPP},i+1}, T_{i+1}\right) + \frac{t - T_i}{T_{i+1} - T_i} VTEC\left(\emptyset_{\mathrm{IPP}}, \lambda'_{\mathrm{IPP},i}, T_i\right) \tag{S5}$$

The accuracy of the linear temporal interpolation from GIMs is governed by the time interval between the SAR acquisition time and the nearest GIM epochs. Smaller time differences reduce interpolation uncertainty, whereas a SAR acquisition time midway between two GIM epochs introduces greater interpolation uncertainty due to the intrinsic variability of ionospheric VTEC.

The TEC along radar slant range or Line-Of-Sight (LOS), hereafter referred to as STEC, is different from VTEC. A mapping function is required to convert VTEC to STEC. We calculate this mapping function as

$$M_{\mathrm{IPP}} = \frac{1}{\cos\theta_{\mathrm{IPP}}} = \frac{1}{\dfrac{X_{\mathrm{IPP}}}{|X_{\mathrm{IPP}}|} \cdot \dfrac{X_s - X_{\mathrm{IPP}}}{|X_s - X_{\mathrm{IPP}}|}} \tag{S6}$$

where M_{IPP} is the mapping function, and θ_{IPP} is the zenith angle at the IPP. Since the true ionosphere is not a thin and homogeneous layer, M_{IPP} is just a first-order approximation of the true mapping function.

Finally, the InSAR ionospheric phase φ_{iono} is computed as

[1] Schaer S, Gurtner W (1998) IONEX: The ionosphere map exchange format version 1. In Proc IGS AC Workshop, Darmstadt, Germany 9:1–12.

$$\varphi_{\text{iono}} = -\frac{4\pi K}{c f_0} VTEC_{\text{IPP},t} \cdot M_{\text{IPP}} \cdot \alpha \tag{S7}$$

where c is the speed of light in vacuum, f_0 is the radar carrier frequency, K is a constant and $K \approx 40.3\ \text{m}^3/\text{s}^2$, and α is a scaling factor that accounts for the difference between GNSS and SAR satellite altitudes. The scaling factor is discussed in detail in Section 4.3.

5 Method for generating the result in the left panel of Fig. 20

We compute the scaling factors by comparing ionospheric phases estimated using the range split-spectrum method with those derived from GIMs. However, this comparison is complicated because the ionospheric phase estimated using the range split-spectrum method is relative in both space and time. The temporal relativeness can be solved by converting the GIM-derived phases to the same relative framework. We select a reference date, and subtract its ionospheric phase from all other dates. Spatial relativity is more challenging to resolve. For each acquisition date, we estimate a constant offset that should be removed from the range split-spectrum estimate to make it spatially absolute. To this end, we use all pixels in the ionospheric phase images from range split-spectrum method and one GIM, and fit a first-order polynomial to get an intercept. This procedure is repeated for all available GIMs, and the constant offset is computed as the mean of the resulting intercepts. This constant offset is then removed from the ionospheric phase estimated using the range split-spectrum method. The entire procedure is repeated independently for each date. After both temporal and spatial relativity are resolved, we compute, for each date, the pixel-wise ratio between the ionospheric phases estimated using the range split-spectrum method and those derived from codg. The final scaling factor is computed by averaging these ratios across all dates. The temporally averaged scaling factor of codg multilooked by 100×100 (range×azimuth) for track A149 is shown in the left panel of Fig. 20. As expected, the scaling factor exhibits clear spatial variations, which are related to changes in acquisition geometry and ionospheric conditions across the scene.

6 Alternative empirical adaptive scaling factor models

A. Long-term polynomial model

$$\begin{aligned}\alpha_{\text{adaptive=}} &- 1.72821862 \times 10^{-19} \cdot date^6 - 1.37912510 \times 10^{-16} \cdot date^5 \\ &+6.34674319 \times 10^{-13} \cdot date^4 + 3.27324972 \times 10^{-10} \cdot date^3 \\ &-8.59751548 \times 10^{-7} \cdot date^2 - 2.72945510 \times 10^{-4} \cdot date \\ &+1.36997812\end{aligned} \tag{S8}$$

where $date$ is the number of days relative to 20191215.

B. Seasonal polynomial model

$$\begin{aligned}\alpha_{\text{adaptive}} &= -1.55109991 \times 10^{-13} \cdot day^6 + 1.70865249 \times 10^{-10} \cdot day^5 \\ &-7.05502999 \times 10^{-8} \cdot day^4 + 1.33509267 \times 10^{-5} \cdot day^3 \\ &-1.10780577 \times 10^{-3} \cdot day^2 + 2.82712511 \times 10^{-2} \cdot day \\ &+1.19878465\end{aligned} \tag{S9}$$

where day is the day of year.

C. Seasonal sinusoidal model

$$\alpha_{\text{adaptive}} = -0.14075397 \times \sin(0.0172 \times day - 0.81424734) + 1.11858188 \quad (S10)$$

where day is the day of year.